DOE/PC/90012-7

# Hydrodynamics of Three-Phase Slurry Fischer-Tropsch Bubble Column Reactors

Quarterly Technical Progress Report

for the Period 1 January 1989 - 31 March 1989

Dragomir B. Bukur, James G. Daly and Snehal A. Patel

Texas A&M University

Department of Chemical Engineering

College Station, TX 77843

April 28, 1989

Prepared for the Pittsburgh Energy Technology Center,

the United States Department of Energy Under Contract No. DE-AC22-86PC90012

George Cinquegrane, Project Manager (PETC)

John Shen, Program Manager (DOE/FE)

DOE/PC/90012-7

# Hydrodynamics of Three-Phase Slurry Fischer-Tropsch Bubble Column Reactors

Quarterly Technical Progress Report

for the Period 1 January 1989 - 31 March 1989

Dragomir B. Bukur, James G. Daly and Snehal A. Patel

Texas A&M University

Department of Chemical Engineering

College Station, TX 77843

April 28, 1989

Prepared for the Pittsburgh Energy Technology Center,

the United States Department of Energy Under Contract No. DE-AC22-86PC90012

George Cinquegrane, Project Manager (PETC)

John Shen, Program Manager (DOE/FE)

## NOTICE



## PATENT STATUS



## TECHNICAL STATUS

TABLE OF CONTENTS

## I. Abstract

We devoted most of our effort to the analysis of data obtained during the earlier hot flow runs in the 0.05 m ID stainless steel bubble column. Axial dispersion coefficients were estimated using data obtained during batch runs with large silica and iron oxide particles. Results from this work are in very good agreement with values reported in literature. We also analyzed wall pressure fluctuations that were measured during the earlier experiments. Time series analysis of the pressure signals showed the transitions from bubbly flow to slug flow in the 0.05 m ID column. There results also showed the flow regimes present at different axial locations in the column at a given gas velocity.

The new high energy Cobalt-60 source was ordered and received during the past quarter. Experiments were made to measure the absorption coefficient for FT-300 wax at several temperatures with and without silica present. We also simulated experiments to test the response of the Cesium-137 source and detector to sudden changes in the void fraction.

## II. Objective and Scope of Work

The overall objective of this contract is to determine the effects of bubble column diameter, solids loading and particle size, and operating conditions (temperature, gas and liquid flow rates) on hydrodynamics of slurry bubble columns for Fischer–Tropsch synthesis, using a molten wax as the liquid medium. To accomplish these objectives, the following specific tasks will be undertaken.

### Task 1 – Project Work Plan

The objective of this task is to establish a detailed project work plan covering the entire period of performance of the contract, including a detailed program schedule, analytical procedures, and estimated costs and manhours expended by month for each task.

### Task 2 – Design and Construction of the Experimental Apparatus

The existing glass and stainless steel columns (0.051 m and 0.229 m in diameter, 3 m tall) that were constructed under our previous DOE contract (DE–AC22–84PC70027), will be modified and additions made in order to study the effect of continuous upward liquid flow. After the procurement of equipment and instrumentation, and construction of the unit is completed, a shakedown of test facilities will be made to verify achievement of planned operating conditions.

### Task 3 – Measurement of Hydrodynamic Parameters by Conventional Techniques

In this task, the effects of operating conditions (liquid and gas superficial velocities, temperature), gas distributor, column diameter, and solids concentrations and particle size on hydrodynamic parameters in the glass and stainless steel columns will be determined. All experiments will be conducted using nitrogen at atmospheric pressure.

The hydrodynamic parameters that will be determined as a function of the independent variables mentioned above are: average gas hold–up, axial solids distribution, axial gas hold–up, flow regime characterization, and qualitative information on bubble size distribution.

Task 4 – Application of a Gamma Radiation Density Gauge for Determining Hydrodynamic Parameters

The objective of this task is to determine hydrodynamic parameters for the three–phase system using a nuclear density gauge apparatus. A movable assembly mechanism and positioning racks for the two nuclear density gauges and detectors will be designed and constructed. Following the interfacing of the apparatus with an on–line microprocessor, the gauges will be calibrated using pure components (liquid wax and solid particles), and with known proportions of liquid and solid. After calibration, the following parameters will be obtained from experiments in the large stainless steel column: axial gas hold–up, axial concentration of solids, and qualitative information on flow regimes and bubble size distributions.

## III. Summary of Progress

During the past quarter we placed an order with Tuthill Corporation of Chicago for a new lobe type positive displacement pump. We expect to receive the pump by the end of April, 1989. The issue with Gelber Pumps related to our existing slurry pump was finally resolved. We have been informed that we will not be charged for the replacement parts that were sent to us in late 1988. Subsequently the pump was rebuilt and reinstalled in the 0.05 m ID column circuit. We also received a shipment of Sasol's Arge reactor wax during the past quarter. We plan to use this wax as the liquid medium in all runs in the 0.23 m ID column and in some runs in the 0.05 m ID column.

We devoted considerable effort during the quarter towards analyzing data collected during earlier hot flow runs in the 0.05 m ID column. Axial dispersion coefficients were estimated and wall pressure fluctuations, measured during the earlier runs, were analyzed.

Axial dispersion coefficients were determined using data from batch mode runs with large (20-44 $\mu$m) iron oxide and silica particles. We did not estimate dispersion coefficients for batch and continuous mode experiments with 0-5 $\mu$m solid particles, since the axial solids concentration profiles for these runs were uniform. For batch experiments, the hindered settling velocity and the dispersion coefficient are unseparable. We therefore used correlations available in literature for the hindered settling velocity, and estimated the dispersion coefficients from our data. When data from the top of the dispersion were omitted, dispersion coefficients were higher than values obtained when all data points were used. This is because the foam present at the top of the dispersion is unable to suspend the solids, causing the solids concentration profile to be steeper. The differences were more pronounced with large iron oxide than they were with large silica particles, because of the relatively greater amount of foam produced with the former. When the effect of foam was discounted, dispersion coefficients for iron

oxide were consistently higher than those for silica. Dispersion coefficients obtained from our study fall within the range of values predicted by correlations available in literature. However, our results appear to indicate that settling velocities for these particles are higher than those predicted by literature correlations, and additional data from continuous mode experiments are necessary before any definite conclusions can be drawn.

We developed the necessary software for doing time series analysis of pressure fluctuations on our AT compatible computer. The root mean square value (RMS), mean square error (MSE), probability density function (pdf), power spectral density function (psd), and the autocorrelation functions were generated for each data set. Flow regime transitions based on the mean square error (MSE) and on the power spectra (psd) are discussed. In all experiments the transition between bubbly and slug flow regimes occurred somewhere between the gas velocities of 0.04 and 0.06 m/s. Our results also indicate the absence of slugs below a height of about 36 inches above the distributor. Power spectra show the change in dominant frequencies with flow regimes and gas velocities. The dominant slug frequency for batch mode runs is around 2.5 Hz at the top of the column. For continuous mode runs, the dominant slug frequency is between 2.5 and 5 Hz. It appears that liquid circulation retards the coalescence of small slugs to form large slugs such as those detected in the batch mode of operation. Power spectra confirm the flow regime transition range to be between gas velocities of 0.04 and 0.06 m/s, as indicated by a definite shift in the dominant frequency.

The new Cobalt-60 source was ordered and received during the past quarter. We are in the process of having a new source holder made; this will be used with the more powerful Cobalt-60 source. We installed the single channel analyzers and measured the absorption coefficient for FT-300 wax at four different temperatures, i.e., 150, 200, 230 and 265°C using the Cesium-137 source. The absorption coefficient decreased from

0.0521 $cm^2/g$ at 150°C to 0.0470 $cm^2/g$ at 265°C, due to the change in wax density with temperature. Absorption coefficients for silica were also measured using 10, 20 and 30 wt.% slurries of silica in FT-300 wax. Absorption coefficients for silica were in the range 0.140-0.148 $cm^2/g$. Experiemnts were made to test the sensitivity of the density gauge apparatus to sudden changes in void fractions. We simulated the process using spinning disks with holes along a circle near the periphery of the disks. When these disks were rotated in the path of the density gauge beam, we were able to use the resulting signal to determine the relevant frequencies precisely. However, further adjustments to the density gauge electronics are necessary before actual experiments can be conducted.

## IV. Detailed Description of Technical Progress

### A. Task 3 – Measurement of Hydrodynamic Parameters by Conventional Techniques

#### A.1. Overview of Bubble Column Operations

During the past quarter, we completed the process of acquiring a new slurry pump following the problems we had with Gelber Pumps, Inc., regarding our existing pump. We received technical information and bids from three vendors for a new pump, and placed an order with the Pump Division of Tuthill Corporation (Chicago) for a lobe type positive displacement pump. We expect to receive the pump by the end of April, 1989.

The issue with Gelber Pumps, Inc., has been resolved. We have been informed that they will not charge us for the pump replacement parts that we had received during November-December 1988. The slurry pump was rebuilt using new parts and was installed in the small (0.05 m ID) stainless steel column circuit. The pump and associated lines have been heat traced and insulated in preparation for additional runs.

During the past quarter, we received a shipment of SASOL's Arge reactor wax from SASOL, South Africa. We plan to use this as the liquid medium for experiments in the large (0.23 m ID) stainless steel column, and for some experiments in the small (0.05 m ID) stainless steel column. We plan to resume experiments in the small column during the next quarter.

#### A.2. Estimation of Axial Dispersion Coefficients

During the past quarter, we completed the analysis of data obtained from earlier runs made in the 0.05 m ID stainless steel column. Hold-up and solids concentration data from two runs conducted in the batch mode of operation, with 20 wt.% of 20-44 $\mu$m iron oxide and silica particles (Quarterly Technical Progress Report for the period 1 July–30 September 1988), were used to estimate the axial dispersion coefficients. Axial dispersion coefficients were not determined for batch and continuous mode experiments with 0-5 $\mu$m particles since solids distributions were uniform in these experiments. Some

problems were encountered during the batch mode experiment with large silica, and the average solids concentration in the column dropped from 20 wt.% to 10 wt.% during the course of the experiment. There were no operational problems during the batch mode experiment with large iron oxide, where the average solids concentration remained at around 20 wt% during the entire run.

A.2a. Theoretical Background

Two models are commonly used to predict solids concentration profiles in bubble column reactors. These are (1) the semi–infinite dispersion model and (2) the finite dispersion model. The former has found widespread use; whereas, the latter model has proven to be inadequate (Chang and Morsi, 1988). The analysis presented here is based on the semi-infinite model.

Several variations of the one-dimensional sedimentation dispersion model, based on different frames of reference, are available in the literature. The model presented by Cova (1966) is based on the cross-sectional area of the column; whereas, the models by Kato et al. (1982), Smith and Ruether (1985), and O'Dowd et al. (1987), are based on the cross-sectional area occupied by the slurry phase alone (i.e., area occupied by the gas phase is not included). In our analysis we have used the model presented by Smith and Ruether. Their one-dimensional axial dispersion model is given by

$$\frac{\delta}{\delta x}\left[\frac{-E_s}{L}\frac{\delta C_s}{\delta x}\right] + \frac{\delta}{\delta x}\left[\left[\frac{U_{s\ell}}{1-\epsilon_g} - \Phi_\ell U_p\right] C_s\right] = L\frac{\delta C_s}{\delta t} \qquad (1)$$

where x is the dimensionless height above the distributor (based on expanded height), $E_s$ is the axial dispersion coefficient, $C_s$ is the solids concentration, $U_{s\ell}$ is the average slurry flow rate, $U_p$ is the hindered settling velocity of the particles, $\Phi_\ell$ is the volume fraction of liquid in the slurry, and t is the time.

For batch mode of operation (i.e., $U_{s\ell}$=0) at steady state (no time derivatives), and assuming no dependency of $\Phi_\ell$ on height (Note: $\Phi_\ell$ varied from 0.94 to 0.98 for

all gas velocities for both experiments), Eq. 1 reduces to

$$\frac{\delta}{\delta x}\left[\frac{-E_s}{L}\frac{\delta C_s}{\delta x}\right] - \frac{\delta}{\delta x}\left[\overline{\Phi_\ell} U_p C_s\right] = 0 \tag{2}$$

where $\overline{\Phi_\ell}$ is the average axial liquid volume fraction in the column. Equation (2) can be integrated twice to yield:

$$C_s = C_1 + C_2 \exp\left[-L\overline{\Phi_\ell}\frac{U_p}{E_s}x\right] \tag{3}$$

For the semi–infinite dispersion model, the boundary conditions are given by: $C_s = 0$ as x approaches infinity, and $C_s = C_s^B$ for $x = 0$, where $C_s^B$ is the concentration of solids at the bottom of the dispersion. Application of these boundary conditions to Eq. (3) yields:

$$C_s = C_s^B \exp\left[-L\overline{\Phi_\ell}\frac{U_p}{E_s}x\right] \tag{4}$$

Solids concentration vs. axial position data can now be used to obtain estimates of $\frac{U_p}{E_s}$ and the initial feed concentration, $C_s^B$, using regression analysis.

For continuous liquid flow, the solution to Eq. 1 is given by:

$$C_s = \left(C_s^B + a\right)\exp\left[-(U_p\overline{\Phi_\ell} - U'_{s\ell})\frac{L}{E_s}x\right] - a \tag{5}$$

where $a = \frac{U'_{s\ell} C_s^f}{\overline{\Phi_\ell} U_p - U_{s\ell}}$ and $U'_{s\ell} = \frac{U_{s\ell}}{(1-\epsilon_g)}$. The quantity $C_s^f$ is the concentration of solids in the feed. It is assumed that no settling occurs in the feed stream (i.e., at $x<0$, $U_p = 0.0$ and $\frac{\delta C_s}{\delta x} = 0.0$). Non linear regression techniques may be used to solve Eq. 5 for $U_p$, $E_s$, and $C_s^B$.

For batch experiments, $U_p$ and $E_s$ are not separable, and in order to obtain axial dispersion coefficients, one must assume values for the hindered settling velocity of the solids. There are various correlations available in the literature for estimating hindered settling velocities (e.g., Kato et al. (1972), Smith and Ruether (1985), Zigrang and

Sylvester (1981), and O'Dowd et al. (1987)). The correlations proposed by Kato et al., Smith and Ruether, and O'Dowd et al. are all of the form

$$U_p = a U_T{}^b U_g{}^c \bar{\Phi}_\ell{}^d \tag{6}$$

The constants in Eq. 6 are (1.33, 0.75, 0.25, 2.5) for Kato et al., (1.91, 0.8, 0.26, 3.5) for Smith and Ruether, and (1.69, 0.8, 0.23, 1.28) for O'Dowd et al. $U_T$ is the terminal rise velocity of a single particle in an infinite liquid medium.

Various correlations have been presented in the literature for predicting axial dispersion coefficients directly. The correlation proposed by Kato et al. is:

$$Pe_p = \frac{13 Fr_g}{1 + 8 Fr_g^{.85}} \tag{7}$$

The equation presented by Smith and Ruether is:

$$Pe_p = 9.6 \left[\frac{Fr_g^6}{Re_g}\right]^{0.114} + 0.019 Re_p^{1.1} \tag{8}$$

and the equation presented by O'Dowd et al. for an unbaffled bubble column is:

$$Pe_p = 7.7 \left[\frac{Fr_g^6}{Re_g}\right]^{0.098} + 0.019 Re_p^{1.1} \tag{9}$$

where $Pe_p = \frac{U_g D_{col}}{E_s}$, $Re_g = \frac{U_g D_{col} \rho_\ell}{\mu_\ell}$, $Fr_g = \frac{U_g}{\sqrt{g D_{col}}}$, and $Re_p = \frac{d_p \rho_\ell U_T}{\mu_\ell}$. The correlation proposed by Kato et al. (Eq. 7) does not include solids concentration or size; however, they have proposed a modified correlation for use with large particles, which does include the particle Reynolds Number

$$Pe_p = \frac{13 Fr_g (1 + 0.009 Re_p Fr_g^{-0.8})}{1 + 8 Fr_g^{0.85}} \tag{10}$$

For systems used in our studies, the correction factor for particle size effect in Eq. 10 was negligible.

A.2b. Discussion of Results

Axial dispersion coefficients were obtained for batch experiments conducted with FT–300 wax as the liquid medium and iron oxide (35 – 44 $\mu$m) and silica (20 – 44 $\mu$m) as the solids phase at 265 °C. Gas velocities of 0.02, 0.04, 0.06, 0.09, and 0.12 m/s were employed for the experiment with iron oxide and gas velocities of 0.12, 0.06, 0.04, and 0.02 m/s (in the given order) were employed for the silica run.

Axial gas hold-up and solids distribution profiles for the two runs are shown in Figures 1 and 2, respectively. For the run with iron oxide, a significant amount of foam was observed in the uppermost section of the column; whereas, the amount of foam was much lower in the experiment with silica particles. For both experiments, there was a significant change in solids concentration with column height. For the iron oxide run, solids concentration ranged from 34 wt% at the bottom of the dispersion to 10 wt% at the top of the dispersion. The abrupt shift in the solids concentration profile for the experiment with silica particles (Figure 1b) was due to operational problems encountered between gas velocities of 0.12 and 0.06 m/s.

Figure 3 shows the effect of superficial gas velocity on the quotient $\frac{U_p}{E_s}$, which was estimated by fitting solids concentration vs. normalized axial height data to Eq. 4. Figures 3a and 3b correspond to values of $\frac{U_p}{E_s}$ obtained using all solids concentration data. Figures 3c and 3d correspond to values of $\frac{U_p}{E_s}$ obtained when solids concentration data from the uppermost sample port were omitted. This was done to eliminate effects due to the presence of foam at the top of the dispersion. Also shown in Figure 3 are the 95 % confidence intervals for the $\frac{U_p}{E_s}$ estimates. The results from our work are compared with those predicted by literature correlations (i.e., $U_p$ from Eq. 6 and $E_s$ from Eqs. 7, 8 and 9) in Figure 4. A slight downward trend in $\frac{U_p}{E_s}$ with increasing gas velocity can be seen in Figure 4. This is expected since higher gas velocities would promote axial mixing of the dispersion and improve solids distribution, resulting in higher $E_s$ values.

Figure 4 also shows that results from our study are within the range of values predicted by the existing correlations. The effect of omitting data from the top most port is more pronounced for the run with iron oxide than for the run with silica. When the reduced data set was used for the experiment with iron oxide, $\frac{U_p}{E_s}$ values were consistently lower than values obtained when all data points were used. Whereas, for the run with silica, values for the two cases were similar. This may be due to the different amounts of foam produced with the two systems. During the run with iron oxide, the amount of foam present at the top of the dispersion was significantly higher than that present during the run with silica. The higher $\frac{U_p}{E_s}$ values in the presence of foam may be attributed to the inability of foam to suspend the solids.

Figures 5 and 6 compare the measured solids concentration profiles with those predicted by the semi–infinite model for the two systems. For the experiment with silica (Figure 5), there is essentially no difference between the predicted values of solids concentration from the two cases studied (i.e., using all data points and omitting the last data point). This is expected since we saw very little difference in $\frac{U_p}{E_s}$ for the two cases (Figure 4). The semi–infinite dispersion model fits the data very well. However, for iron oxide, (Figure 6) there is some difference between the predicted solids concentration curves for the two cases. For the case where all points are used, there is a steeper concentration gradient predicted, possibly due to the presence of foam in the upper section.

Figure 7 compares hindered settling velocity values calculated from the three correlations (Eq. 6), for both silica and iron oxide. The effect of superficial gas velocity on hindered settling velocity is evident from Figure 7. The values remain fairly constant for silica when compared to those for iron oxide.

Figures 8–10 show results for axial solids dispersion coefficients based on the three point (closed symbols) and four point (open symbols) least square fit of the data to

the semi-infinite dispersion model for both iron oxide (top) and silica (bottom). Values predicted by Eqs. 7–9 are also shown on the figures. Figure 8 shows our results based on Kato's correlation for settling velocity. Our results shown in Figure 9 are based on Smith and Ruether's correlation for settling velocity. Values of $E_s$ calculated using O'Dowd et al.'s correlation for settling velocity in an unbaffled column are shown in Figure 10. For iron oxide, the dispersion coefficients obtained using all data points for solids concentration were lower than the dispersion coefficients obtained when the solids concentrations corresponding to the uppermost sample port were omitted. The difference in dispersion coefficients based on the two fits are most significant at higher gas velocities. At a gas velocity of 0.02 m/s there is essentially no difference in the dispersion coefficients. An interesting observation is that for the silica run, in which little foam was produced, the dispersion coefficients determined using all data points were similar to those obtained when data from the uppermost port were omitted. The dispersion coefficients obtained for iron oxide based on data analysis when the uppermost solids concentration sample was omitted were consistently higher than those for silica. However, for the case where all data points are used, the values of dispersion coefficients for silica and iron oxide are similar. The dispersion coefficients obtained using Kato et al.'s correlation for settling velocity were lower than those predicted directly using Kato et al.'s equation for the dispersion coefficient (i.e., Eq. 7) (see Figure 8). Dispersion coefficients obtained using Smith and Ruether's correlation for settling velocity were higher than those predicted using their equation for dispersion coefficients (Eq. 8). Results based on O'Dowd et al's correlation for $U_p$ also were higher than those obtained using their correlation for $E_s$ (Eq. 9). Results from our study fall within the range of values predicted by the various correlations.

In order to improve the estimates of the dispersion coefficient, we decided to modify the correlation of the form shown in Eq. 6 by fitting our data to it and estimating the

coefficient. We retained the exponents proposed by Kato et al. (their correlation is based on an extensive data base). Using $E_s$ from Eq. 7, hindered settling velocities ($U_p$) were calculated from the measured values of $\frac{U_p}{E_s}$. These values were then used to estimate a new value of the coefficient in Eq. 6 in the least squares sense. If we used only the iron oxide data, we obtained a value of 1.97 for the coefficient, and if we used only the silica data, we also obtained a value of 1.97. This is higher than the value of 1.33 given by Kato. Figure 11 is a parity plot of measured dispersion coefficient versus values predicted using Kato's correlation for dispersion coefficients and our data based on the modified form of Kato's equation for settling velocity. The broken lines represent a $\pm 8\%$ band. With this modification for the settling velocity, there is excellent agreement between the predicted and measured dispersion coefficients.

The settling velocities predicted using the modified form of Kato's equation (i.e., using a coefficient of 1.97 in Eq. 6) are compared with the settling velocities predicted by literature correlations in Figure 12. The settling velocities required to satisfy Eq. 7 (i.e. solid line in Figure 12) are higher than settling velocities predicted by the other correlations. This is possibly because our settling velocities are actually higher. Brian and Dyer, (1984) conducted experiments to determine axial dispersion coefficients for different size distributions of iron oxide and silica in isoparaffin. The isoparaffin used in their study had physical properties similar to those of the FT–300 wax used in this study. One of the particle size distributions studied was 44 – 53 $\mu$m particles which is very close to that used in the present study. They obtained hindered settling velocities from experiments conducted in the continuous mode of operation. Settling velocities from their study with the 44 – 53 $\mu$m particles of silica were substantially higher than those predicted by Eq. 6 using constants from Kato's work, and in some cases were even higher than those obtained for iron oxide particles of the same size. They did not postulate a reason for the trends observed with their measured values. Settling velocities

from our study could be as high as those obtained by Brian and Dyer; however, actual measurements with our systems would be necessary to verify this.

## A.3. Statistical Analysis of Wall Pressure Fluctuations

We have analyzed pressure fluctuation signals that were recorded during earlier experiments in the 0.05 m ID bubble column. We developed the necessary software that would allow us to do time series analysis of the signals on the Zenith-248 AT compatible computer in our laboratory. The same computer is also interfaced to the data acquisition system that was used to record the pressure fluctuations.

### A.3a. Theoretical Background

Statistical analysis of pressure fluctuations has been used in the past to determine transitions between flow regimes in both two–phase and three–phase bubble columns and fluidized beds. Various techniques may be used to determine flow regimes and flow regime transitions. The two most commonly used designs involving pressure transducers are: (1) measurement of absolute pressure fluctuations and (2) measurement of differential pressure fluctuations. For analysis of systems which operate in the slug flow regime, differential pressure fluctuations can provide more detailed information, and a more accurate measure of the transition from bubbly to slug flow, slug flow to annular flow, and annular flow to mist flow. Differential pressure measurements have generally been limited to two–phase systems (e.g., Ishigai et al. 1965a & b, Lin and Hanratty 1987, Matsui 1984, Miyazaki et al. 1973, Akagawa 1971a, b & c, etc.). These measurements may be used to determine instantaneous fluctuations in void fraction. The signals returned from differential transducers have the same characteristics as those obtained from a nuclear density gauge or a probe.

Surface pressure fluctuations may be detected with various types of pressure measurement equipment (e.g., pitot tubes, surface mounted transducers, microphones,

transducers connected by an external tube, etc.). One drawback associated with surface mounted and tube mounted transducers is that they respond to fluctuations occurring not only in the boundary layer, but also to fluctuations beyond the boundary layer. The tube mounted transducers also suffer from signal delay governed by the length of the tube and the velocity of sound in the medium. With tube mounted transducers, it is usually difficult to obtain data over the entire range of frequencies. In general, data obtained from tube mounted transducers will be limited to low frequency fluctuations in the system. For our purpose, this should be sufficient since we are interested in detecting the onset of slug flow.

As discussed by Glasgow et al. (1984), the passage of a buoyant bubble can produce three distinct response characteristics: (1) sound of approach (observable if rapidly rising bubbles are present), (2) pressure field around the object, and (3) wake or vortex street behind the object. Our pressure transducers will only detect fluctuations caused by changes in the pressure field as a bubble passes the surface of the tube (i.e., low frequency oscillations). Even if our system was sensitive enough to detect fluctuations caused by the wakes of bubbles, it would be very difficult, if not impossible, to distinguish between these fluctuations and those created by the pressure field around the bubble.

Three different statistical techniques are commonly employed to determine flow regimes and flow regime transitions from pressure transducer measurements. The statistical analysis involves the use of the power spectral density function (psd), the mean square error of the pressure fluctuations (MSE), and the probability density function (pdf). The pdf is used extensively in the analysis of signals obtained from differential transducers, nuclear density gauges, and probes. Flow regimes and flow regime transitions cannot be determined directly from pdf's for data obtained from absolute pressure measurements.

For data from differential pressure measurements, the pdf has significantly different

characteristics for different flow regimes. In bubbly flow the pdf is concentrated near a pressure difference corresponding to low gas hold–up. However, when slugs begin to appear, two peaks (or regions) are observed on the pdf curve, one corresponding to low hold–up and the other corresponding to high hold–up. The low hold–up region corresponds to the liquid slugs and the high hold–up region corresponds to the gas slugs. In annular flow, the low hold–up peak disappears and only the peak corresponding to high gas hold–up is observed.

As mentioned previously, the pdf of an absolute pressure signal cannot be used as a direct measure of flow regime transitions. However, the pdf of an absolute pressure signal will broaden as turbulence increases. In other words, the variance of the pressure fluctuations in the column changes with gas and liquid velocities, and this change is reflected by an increase or decrease in the variance of the pdf. Two quantities which have found some use in determining flow regime transitions and changes in turbulence are the mean square error (MSE) and root mean square (RMS) of the pressure fluctuations. The MSE is defined as:

$$MSE = \frac{\left[\sum (P_i - \overline{P})^2 / N\right]^{1/2}}{\overline{P}} \qquad i = 1, \ldots, N \tag{11}$$

where N is the total number of data points, $P_i$ is the pressure corresponding to data point i, and $\overline{P}$ is the average pressure defined as:

$$\overline{P} = \frac{\sum P_i}{N} \qquad i = 1, \ldots, N$$

Fan et al. (1984) had reasonable success in using this quantity to determine flow regime transitions in a three–phase fluidized bed. Lee (1983) used the RMS, defined as :

$$RMS = (MSE)(\overline{P}) \tag{12}$$

to obtain a qualitative description of turbulence in an air lift bubble column.

Two other statistical quantities which are sometimes used are the autocorrelation function and the power spectral density function (psd). The psd is the Fourier transform of the autocorrelation function. The autocorrelation function is the normalized autocovariance function. The autocovariance function gives an indication of how the dependence between adjacent values in a stochastic process changes with lag (u) and is defined as:

$$\gamma_{xx}(u) = E[(x(t) - \mu)(x(t+u) - \mu)] = cov[x(t), x(t+u)] \tag{13}$$

where E[y] is the expected value of y, cov is the covariance, $\mu$ is the mean of the time series, x is the measured quantity (pressures for our case), and u is the lag between observations. The autocorrelation function is given by:

$$\rho_{xx}(u) = \frac{\gamma_{xx}(u)}{\gamma_{xx}(0)} \tag{14}$$

where $\gamma_{xx}(u)$ is the autocovariance function evaluated at lag u and $\gamma_{xx}(0)$ is the autocovariance function evaluated at lag 0, or more simply, the variance of the time series. Thus, the RMS is the square root of the autocovariance function evaluated at lag 0, and the MSE is the square root of the autocovariance function evaluated at lag 0 divided by the mean of the time series (or, for our case, the mean of the pressure fluctuations).

Fourier transforms are used to approximate the time series. A series of periodic functions may be used to approximate a non–periodic signal. One such series is the Fourier series, in which the periodic functions are sines and cosines. Thus, the Fourier series may be used to approximate the actual pressure signal. In essence, we are fitting the raw signal to a Fourier series. From this type of a fit, we gain information on the periodicity of the signal. Fourier series have the important property that an approximation consisting of a given number of terms achieves the minimum mean square error between the signal and approximation, and also, since they are orthogonal, the

coefficients may be determined independently of one another. The sample spectrum is the Fourier transform of the sample autocovariance function. It shows how the average power or variance of the signal is distributed over frequency. Fourier analysis breaks down when applied to time series because it is based on the assumption of fixed amplitudes, frequencies, and phases. Thus, the sample spectrum of a time series can be quite erratic in nature. However, if we treat the sample spectrum as a random variable, and examine its moments, we will be able to explain the erratic behavior. The power spectrum is defined as the first moment, or mean, of the sample spectrum. The power spectral density function is a normalized version of the power spectrum. The psd is the Fourier transform of the autocorrelation function and is defined by:

$$P(f) = \int_{-\infty}^{\infty} \rho_{xx}(u)\exp(-j2\pi fu)du \tag{15}$$

Thus, all three quantities (i.e., RMS or MSE, autocorrelation and psd) are related. For our data, we will only use the MSE and psd to show qualitatively, the transitions between flow regimes for various experimental data.

Taitel et al. (1980) presented various correlations for the prediction of flow regime transitions in two–phase gas–liquid flow. By treating our three–phase system as a two–phase system (i.e., using slurry properties in place of liquid properties), we can use Taitel et al.'s correlations to obtain approximate values for the transitions between bubbly and slug flow. According to Taitel et al., for our system and range of operating conditions there are two possible flow regimes which can exist, bubbly and slug flow. Taitel et al. also present a correlation for describing the entrance region in which churn flow will exist (i.e., in the lower section of the column there will be churn flow, but towards the top of the column slug flow will exist).

According to Taitel et al., bubbly flow will not exist if the following correlation is

satisfied:

$$\left[\frac{\rho_{s\ell}^2 g D_{col}^2}{(\rho_{s\ell}-\rho_g)\sigma}\right]^{1/4} \leq 4.36 \qquad (16)$$

where $\rho_{s\ell}$ is the density of the slurry, $D_{col}$ is the column diameter, $\rho_g$ is the density of the gas, and $\sigma$ is the surface tension of the liquid. Note that in their original correlation they used the density of the liquid and not the density of the slurry. For our system, the quantity on the left hand side of Eq. 16 ranges from approximately 5.2 to 5.5. Thus, for our system, according to Taitel et al., it is possible to observe the bubbly regime.

Assuming that the transition to slug flow occurs when the gas hold–up is approximately 25 %, Taitel et al. propose that the following correlation can be used to determine the transition to slug flow:

$$U_{s\ell} = 3.0U_g - 1.15\left[\frac{g(\rho_{s\ell}-\rho_g)\sigma}{\rho_{s\ell}^2}\right]^{1/4} \qquad (17).$$

where $U_{s\ell}$ is the superficial slurry velocity and $U_g$ is the superficial gas velocity at which the transition takes place. For the various systems and operating conditions used in this study, the transition from the bubbly to slug flow regime should occur between gas velocities of 0.048 and 0.056 m/s.

Taitel et al. also present a correlation for predicting the entry region over which churn flow will exist. In this region, it is assumed that short Taylor bubbles are created. Two of these coalesce to form a "large" Taylor bubble (or slug). The entry region is the region in which this coalescence takes place and is defined by:

$$\frac{l_e}{D_{col}} = 40.6\left[\frac{U_m}{\sqrt{gD_{col}}} + 0.22\right] \qquad (18)$$

For our system, the entry length, $l_e$ ranges from approximately 2 feet at a gas velocity of 0.06 m/s to 3 feet at a gas velocity of 0.12 m/s. Thus, if Taitel et al.'s correlations (i.e., Eqs. 17 and 18) hold true for our system, we should observe a transition to slug flow between gas velocities of 0.04 and 0.06 m/s for all experiments, and furthermore, we should not observe slugs in the lower (2 to 3 feet) section of the bubble column.

A.3b. Discussion of Results

Wall pressure fluctuations were measured at various axial locations along the column (see Figure 13 for details). The pressure taps will be referred to as 1, 2, 3, 4, and 5. For experiments conducted in the batch mode of operation, cells 1 – 4 were used and for experiments conducted in the continuous mode of operation, cells 1 – 5 were used. Experiments were conducted with small silica particles (0 – 5 $\mu$m) and large iron oxide (44 – 53 $\mu$m) particles at gas velocities of 0.02, 0.04, 0.06, and 0.09 and/or 0.12m/s. Liquid flow rates of 0.0, 0.05, and 0.2 m/s were used in the various experiments. Pressure signals were recorded at 50 Hz for 20 seconds (i.e., 1000 data points per set).

Figures 14 – 16 show typical probability density functions of the pressure signals. The results are from Run F515-FEL10-2S. Figure 14 corresponds to the bubbly flow regime and Figures 15 and 16 correspond to the slug flow regime. In the slug flow regime, the pressure variation is significantly greater than that in the bubbly flow regime. In particular, for this experiment, the pressure varied from 21.5 to 25.5 inches of water in the slug flow regime at a gas velocity of 0.12 m/s (Figure 16) and only from 34 to 35 inches of water in the bubbly regime (Figure 14). Statistical analysis (i.e., MSE and psd) of the pressure signals was used to determine transitions from bubbly to slug flow.

Flow regime transitions based on the MSE:

MSE were calculated from the raw pressure signal data for all runs conducted. In general, the MSE increased with increasing gas velocity and with increasing height above the distributor, but decreased with increasing liquid velocity. Figure 17 shows the MSE obtained from pressure transducer number three for experiments F432–SIS20–2S, F440–SIS20–2S, and F455–SIS30-2S. At low gas velocities (i.e., $U_g \leq 0.06$ m/s, the MSE of the pressure fluctuations is essentially the same for all three experiments. However, at gas velocities of 0.09 and 0.12 m/s the MSE of the pressure fluctuations are significantly different for the various experiments. The MSE for Run F440–SIS20–2S,

which was conducted in the batch mode of operation is significantly higher than those for the other two runs, which were conducted in the continuous mode of operation. This increase in MSE for the batch experiment may be attributed to an increase in turbulence at the top of the dispersion due to fluctuations caused by slugs exiting the slurry. The MSE for Run F455–SIS30–2S, was higher than that for Run F432–SIS20–2S. Increasing the liquid velocity causes a decrease in pressure fluctuations. This decrease in the variance of pressure fluctuations with increasing slurry flow rate may be attributed to two factors: (1) the relative velocity between the gas and slurry decreases with increasing slurry velocity and (2) the static height of the slurry above a given pressure port does not fluctuate as much during a continuous run as it does during a batch run. In Figure 17 there is a distinct change in the slope of the curves between gas velocities of 0.02 to 0.04 m/s and 0.06 to 0.12 m/s. This change in slope may be attributed to a change in the flow regime from bubbly to slug flow. It appears that the transition occurs somewhere between gas velocities of 0.04 and 0.06 m/s for all three experiments. Similar trends were observed in all other experiments conducted. This result agrees with the transition velocities predicted from Taitel et al.'s correlation (i.e., Eq. 17).

Figure 18 shows the effect of height above the distributor on the MSE at various gas velocities for run F440-SIS20-2S. In general, the MSE increases with increasing $U_g$ for all pressure transducers. One interesting trend was the decrease in the MSE for pressure transducer 2 as compared to transducer 1. We cannot be certain of the cause for the decrease in MSE at gas velocities of 0.09 and 0.12 m/s. One possible explanation is that the increase in oscillations at pressure transducer 1 is due to the increase in turbulence near the distributor caused by the increase in the gas velocity. The sharp changes in the slope of the MSE curve between pressure ports 2 and 3 at gas velocities of 0.06, 0.09, and 0.12 m/s indicates that slugs begin appearing in the column somewhere between heights of 24 and 48 inches above the distributor. At gas

velocities of 0.02 and 0.04 m/s, there is a slight change in the slope of the MSE curve between pressure ports 3 and 4, indicating the presence of large bubbles or slugs at a height of 72 inches above the distributor. This result agrees with the prediction of Eq. 18, i.e., slugs will not develop in the bottom part of the column.

Figure 19 shows the effect of superficial gas velocity on the MSE of the pressure fluctuations from Run F440–SIS20–2S. At pressure transducers 1 and 2, we do not observe a transition to slug flow; however, the change in slope of the MSE curve for transducer number 3 between gas velocities of 0.04 and 0.06 m/s indicates a transition to slug flow between these velocities. On the other hand, the slope of the MSE curve corresponding to transducer number 4 does not change significantly, indicating that large bubbles are present at all velocities at a height of 6 feet above the distributor.

Results obtained from experiments with large iron oxide particles showed similar trends in the MSE with gas velocity and height above the distributor. In general, for all experiments in which pressure fluctuations were obtained, the transition between bubbly and slug flow occurred somewhere between gas velocities of 0.04 and 0.06 m/s. Also, slugs were not observed below a height of 36 inches above the distributor.

Flow regime transitions based on the psd:

Pressure signals required high pass filtering. Slow changes in the mean of the pressure signal, unrelated to higher frequency hydrodynamic phenomena, gave rise to a heavy low frequency bias in the psd and autocorrelation functions. To avoid this, the first difference of the time series corresponding to pressure fluctuations was used before spectra were obtained. The first difference is defined as:

$$P'_t = P_{t+\Delta t} - P_t \tag{19}$$

The psd of data from experiments with small silica particles and large iron particles were obtained. The results from these calculations were used to determine flow regime

transitions and slug frequencies. Results obtained from experiments with large iron oxide particles are discussed here, results from experiments with small silica particles were similar.

The three experiments conducted with large iron oxide particles were F515-FEL10–2S, F522–FEL10–2S, and F540–FEL20–2S. In the two continuous runs, the average solids concentration in the column was approximately 5 wt%, and in the batch run, the average solids concentration was 20 wt%. Power spectral density functions are not shown for pressure transducer number 1 since it is located only 3 inches above the distributor and did not show any significant trends with regard to transitions in flow regimes.

Figures 20, 21, and 22 are the psd's for pressure transducers 3, 4, and 5 for run F515–FEL10–2S. At a gas velocity of 0.02 m/s, the frequency spectra for pressure transducers 3 and 4 are fairly broad, with frequencies ranging from 2.5 to 10 Hz. The peaks observed around 10 Hz were present at all gas velocities and had approximately the same intensity. We believe these peaks are due to noise in the system, either from the pump or from the stirrer on the storage tank. For gas velocities of 0.04, 0.06, and 0.09 m/s, the dominant frequencies are lower, i.e., in the range 2.5 and 5.0 Hz. The intensity of the psd increases with increasing gas velocity; a similar trend was observed with the MSE (i.e., increase in MSE with increase in gas velocity). The intensity of the fluctuations was greater at pressure port number 4 than at pressure port number 5. Foam was present in the uppermost section of the column (i.e., at transducer number 5). Since foam tends to dampen the oscillations we believe this is what caused the decrease in intensity at transducer number 5 compared to transducer number 4.

Figure 23 shows the psd's generated at transducer number 4 for Run F522–FEL10–2S. The spectra are similar to those obtained from Run F515–FEL10–2S. However, at a gas velocity of 0.04 m/s the spectrum is still quite broad, with frequencies ranging

from 2.5 to 10 Hz. At gas velocities of 0.06 and 0.09 m/s, the dominant frequency is in the range 2.5 to 5 Hz, which is similar to that observed in run F515–FEL10–2S. This shift in frequency is an indication of the onset of slug flow between gas velocities of 0.04 and 0.06 m/s.

Figure 24 shows the spectra associated with run F540–FEL20–2S for pressure transducer number 4. At lower gas velocities (i.e., $U_g \leq 0.04$ m/s the spectrum is fairly broad with frequencies ranging between 2.5 and 7.5 Hz. However, there is a definite shift to a dominant frequency of approximately 2.5 Hz at higher gas velocities. This indicates that the transition to slug flow occurs between gas velocities of 0.04 and 0.06 m/s. The spectra from transducers 2, 3, and 4 at a gas velocity of 0.12 m/s are shown in Figure 25. The dominant frequency observed at pressure port number 2 is 5 Hz; whereas, the dominant frequency at pressure ports 3 and 4 is approximately 2.5 Hz. This shift from 5 Hz to at the bottom of the column to 2.5 Hz at the top of the column is an indication of coalescence which may be taking place. Similar results were observed for the batch experiment with small silica (see Figure 26). For experiments conducted in the glass column during our previous contract (DE-AC22-84PC70027), we observed slug frequencies in the range 2 to 3 Hz at the top of the column for gas velocities of 0.07, 0.09, and 0.12 m/s. At the bottom of the column, we have more frequent, smaller slugs, whereas, towards the top of the column, two small slugs coalesce to form a single large slug. This type of behavior has been observed visually in our two–phase experiments conducted in the glass column. This also agrees with the description proposed by Taitel et al. which was used in their correlation for determining the entry region over which churn flow exists.

Thus, for experiments conducted in the small stainless steel column in the batch mode of operation, the dominant slug frequency is approximately 2.5 Hz at the top of the column. Coalescence of small slugs to form large slugs occurs between a height

of 2 feet and 4 feet above the distributor. Furthermore, based on the results from the continuous experiments, in which the dominant slug frequency was between 2.5 to 5 Hz, it appears that liquid circulation tends to retard the coalescence of small slugs. Similar results and slug frequencies were observed in the silica experiments. The definite shift in the dominant frequency observed between gas velocities of 0.04 and 0.06 m/s for all experiments indicates that slug flow begins somewhere between these two velocities. As mentioned previously, the same transition region was observed in the silica experiments using MSE analysis. Hence, both MSE and psd analysis may be used to determine the transition from bubbly to slug flow. In addition, the psd may be used to determine slug frequency. There was excellent agreement between results obtained using statistical analysis and both those predicted by Taitel et al.'s correlations and those from our visual observations in the small glass column.

B. Task 4 – Application of a Gamma Radiation Density Gauge for Determining Hydrodynamic Parameters

During the past quarter, we ordered and received a new 35 mCi Cobalt-60 source. As discussed in our last Technical Progress Report (October 1–December 31, 1988), we have found that the Americium-241 source is unsuitable for our application. The new source will be used as the high energy source, whereas the Cesium-137 source, which we already have, will be used as the low energy source. The new source requires a new source holder because of its higher strength. We have designed the source holder and it is being fabricated. Additional lead shields have been received and will be installed before the high energy Cobalt-60 source is used. The two single channel analyzers (SCA) received during the previous quarter have been installed and tested.

B.1 Measurement of Absorption Coefficients

The small stirred tank, used for obtaining absorption coefficients for the three phase system (air-water-sand; Technical Progress Report for the Period October 1–December 31, 1988), was heat traced and insulated for use at higher temperatures. The absorption coefficient measurements for FT-300 wax were made at four different temperatures, i.e., 150, 200, 230 and 265°C to study the effect of wax density on the absorption coefficient. These measurements were made using the Cesium-137 source. The absorption coefficient for pure FT-300 wax decreased with an increase in temperature, and its values at the four different temperatures were 0.0521, 0.0496, 0.0486, and 0.0483, respectively. The linear variation in the absorption coefficient with wax density is as expected.

Absorption coefficients were also measured for slurries of FT-300 wax and 0-5 $\mu$m silica particles with solids loadings of 10, 20, and 30 wt.%. Sample withdrawn from the slurry yielded solids concentrations of 10.5, 18.6 and 26.7 wt% for slurries containing 10, 20, and 30 wt%. solids, respectively. Based on the measured weight fractions and the absorption coefficients fo pure FT-300 wax at 265°C, absorption coefficients for silica were estimated for each solids loading. The absorption coefficients for silica increased with an increase in solids concentration, from 0.140 at 10 wt.% solids to 0.149 at 30 wt.%. The reason for this increase is not known, since one would expect the absorption coefficient to remain constant, irrespective of the solids concentration.

B.2 Density Gauge Response Time Simulations

We conducted tests to determine the response time of the density gauge to sudden changes in the hold-up structure. Since the density gauge measures the local dispersion coefficient of the dispersion, it is desirable to have a response time that is small enough to sense the changes in the path of the beam caused by rapidly moving bubbles. It should be noted that while a faster response time would make it possible to detect rapidly moving large bubbles, the sensitivity to smaller bubbles is dependent more on

the beam width than it is on the response time.

Two 22" diameter stainless steel disks were used in the simulations. In one of the disks, several rectangular slits were made along a 17" diameter circle. The slits were equally spaced along the circumference of the circle and were of the same size. The space between the holes was layered with lead to prevent any passage of radiation through the plate. The second plate was made in a similar fashion, except that the slits were of different widths. The first plate was used to simulate the rise of bubbles of a constant size across the path of the beam, whereas the second plate was used to simulate the passage of a wider bubble size distribution. During a given test, a plate was mounted on a variable speed motor and was positioned between the Cesium-137 source and the detector, so that the path of the beam was perpendicular to the plane of the plate. The plates were then rotated at a predetermined RPM and the signal from the detector was recorded.

We used time series analysis to obtain the autocorrelations and frequency spectra of the signals. For an ideal system we would expect the frequency spectra to show a spike at a frequency corresponding to the rate at which the slits in the plate intersected the beam (for the first plate). Our results do indicate that the density gauge was able to correctly determine the frequency at which the slits passed through the beam. We conducted tests at RPM values that corresponded to a linear velocity of as high as 130 cm/s (i.e., the velocity at which a rectangular slit on the spinning plate passed across the path of the beam). Actual bubble rise velocities in the dispersion are expected to be lower than this value. We can therefore conclude that the density gauge should be able to sense the changes in the hold-up structure caused by the passage of rapidly moving bubbles. We next attempted to use the signals to determine the width of the slits that were intersecting the beam. Once again, for an ideal system, the length of time during which the detector receives a continuous signal should be equal to the time it takes for

a slit in the rotating plate to cross the beam. However, our results showed that at the high velocities at which we conducted the experiments (linear velocity of 130 cm/s) we were not able to predict the width of the slits precisely. This is because the signal did not show a step change in intensity when the leading edge of the slit intersected the beam, instead, the change in intensity was more gradual. Similarly when the trailing edge of the beam passed the beam, the intensity did not drop rapidly. The response was much faster at lower RPM values than it was at higher speeds. We plan to conduct further tests with this set-up using both sources (Cesium-137 and Cobalt-60), and make the necessary adjustments to the density gauge electronics before conducting the actual experiments.

## V. Nomenclature

| | |
|---|---|
| a, b, c, d | constants in Eq. 6, or $a=\frac{U'_{s\ell}C_s^f}{\Phi_\ell U_p - U_{s\ell}}$ in Eq. 5 |
| $C_1$, $C_2$ | constant of integration in Eq. 3 |
| $C_s$ | solids concentration, $g/cm^3$ |
| $C_s^B$ | solids concentration at the bottom of the dispersion, $g/cm^3$ |
| $C_s^f$ | solids concentration in the feed, $g/cm^3$ |
| $d_p$ | particle diameter, cm |
| $D_{col}$ | column diameter, cm |
| $E_s$ | axial dispersion coefficient, $cm^2/s$ |
| $Fr_g$ | Froude number $= \frac{U_g}{\sqrt{gD_{col}}}$ |
| g | acceleration due to gravity, $cm/s^2$ |
| $l_e$ | entry length, cm |
| L | expanded height of the dispersion, cm |
| MSE | mean square error, Eq. 11 |
| N | number of data points |
| psd | power spectral density function |
| P | Fourier transform of the autocorrelation function, Eq. 15 |
| $\overline{P}$ | average pressure |
| $P_i$ | pressure |
| $Pe_p$ | particle Peclet number $= \frac{U_g D_{col}}{E_s}$ |
| $Re_g$ | Reynolds number $= \frac{U_g D_{col}\rho_\ell}{\mu_\ell}$ |
| $Re_p$ | particle Reynolds number $= \frac{U_T d_p \rho_\ell}{\mu_\ell}$ |
| RMS | root mean square, Eq. 12 |
| t | time, s |
| u | lag |

| | |
|---|---|
| $U_g$ | superficial gas velocity, cm/s |
| $U_p$ | hindered settling velocity of particles, cm/s |
| $U_{s\ell}$ | superficial slurry velocity, cm/s |
| $U'_{s\ell}$ | $= \frac{U_{s\ell}}{(1-\epsilon_g)}$ in Eq. 5, cm/s |
| $U_T$ | terminal rise velocity of a single particle in an infinite medium, cm/s |
| x | dimensionless height above the distributor, cm |

Greek letters

| | |
|---|---|
| $\alpha$ | phase weight fraction |
| $\epsilon_g$ | gas phase hold-up |
| $\mu$ | mean of the time series |
| $\mu_\ell$ | liquid viscosity, N.s/m |
| $\rho_\ell$ | liquid density ($g/cm^3$) |
| $\rho_{s\ell}$ | slurry density ($g/cm^3$) |
| $\rho_g$ | gas density ($g/cm^3$) |
| $\rho_{xx}$ | autocorrelation function |
| $\gamma_{xx}$ | autocovariance function |
| $\Phi_\ell$ | volume fraction of liquid in the slurry |
| $\overline{\Phi_\ell}$ | average volume fraction of liquid in the slurry |

## VI. References


Akagawa, K, H. Hamaguchi, and T. Sakaguchi, "I. Studies on the fluctuation of pressure drop in two-phase slug flow," Bull. JSME, 14, 447 (1971a).

Akagawa, K, H. Hamaguchi, and T. Sakaguchi, "II. Studies on the fluctuation of pressure drop in two-phase slug flow," Bull. JSME, 14, 447 (1971b).

Akagawa, K, H. Hamaguchi, and T. Sakaguchi, "III. Studies on the fluctuation of pressure drop in two-phase slug flow," Bull. JSME, 14, 447 (1971c).

Brian, B. W., and Dyer, P. N., "The effect of gas and liquid velocities and solid size on solid suspension in a three-phase bubble column reactor," Chemical and Catalytic Reactor Modeling, Ed. M. P. Dudukovic and P. L. Mills, ACS Symposium Series, 273, 107 (1984).

Chang, M.-Y., and B. I. Morsi, "Gas holdup and axial solid distribution in a slurry bubble column with non-Newtonian fluids," Paper 45d presented at AIChE Annual Meeting, Washington, DC (1988).

Cova, D. R., "Catalyst suspension in gas-agitated tubular reactors," Ind. Eng. Proc. Des. Dev., 5, 20 (1966).

Fan, L. S., S. Satija, and K. Wisecarver, "Pressure fluctuation measurements and flow regime transitions in gas-liquid-solid fluidized beds," Paper 67E presented at AIChE Annual Meeting (1984).

Glasgow, L. A., L. E. Erickson, C. H. Lee, and S. A. Patel, "Wall pressure fluctuations and bubble size distributions at several positions in an airlift fermentor," Chem. Eng. Comm., 29, 311 (1984).

Ishigai, S., M. Yamane, and K. Roko, "Measurement of the component flows in a vertical two-phase flow by making use of the pressure fluctuation: Part I," Bull. JSME, 8, 375 (1965a).

Ishigai, S., M. Yamane, and K. Roko, "Measurement of the component flows in a vertical two-phase flow by making use of the pressure fluctuation: Part II," Bull. JSME, 8, 375 (1965b).

Kato, Y., A. Nishiwaki, T. Fukuda, and S. Tanaka, "The behavior of suspended solid particles and liquid in bubble columns," J. Chem. Eng. Jap., 5, 112 (1972).

Lee, C. H., "Dynamics of bubble size distribution and wall pressure fluctuations in airlift fermentors," Masters Thesis, Kansas State University (1983).

Lin, P. Y., and T. J. Hanratty, "Detection of slug flow from pressure measurements," Int. J. of Multiph. Flow, 13, 13 (1987).

Matsui, G., "Identification of flow regimes in vertical gas-liquid two-phase flow using differential pressure fluctuations," Int. J. Multiph. Flow, 10, 711 (1984).

Miyazaki, K, K. Isogai, Y. Fujii-e, and T. Suita, "Measurement of propagation velocities of pressure and void cross-correlation fluctuations in nitrogen-water flow," J. of Nucl. Sci. Tech., 10, 323 (1973).

O'Dowd, W., D. N. Smith, J. A. Ruether, and S. C. Saxena, "Gas and solids behavior in a baffled and unbaffled slurry bubble column," AIChE J., 33, 1959 (1987).

Smith, D. N., and J. A. Ruether, "Dispersed solid dynamics in a slurry bubble column," Chem. Eng. Sci., 40, 741 (1985).

Taitel, Y., D. Bornea, and A. E. Dukler, "Modelling flow pattern transitions for steady upward gas-liquid flow in vertical tubes," AIChE J., 26, 345 (1980).

Zigrang, D. J., and N. D. Sylvester, "An explicit equation for particle settling velocities in solid-liquid systems," AIChE J., 27, 1043 (1981).

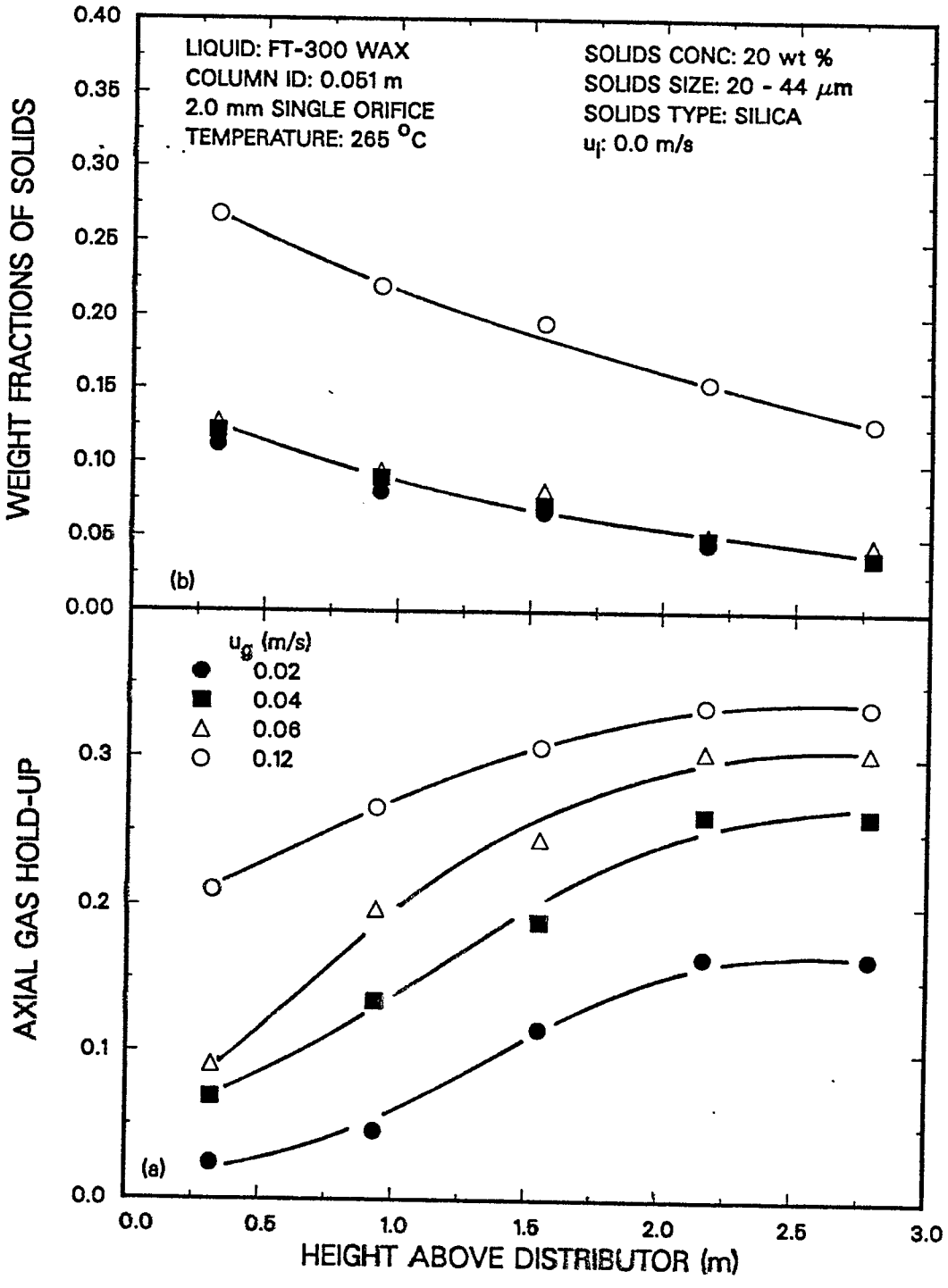


Figure 1. Effect of superficial gas velocity on axial solids distribution (top) and on axial gas hold-up (bottom).

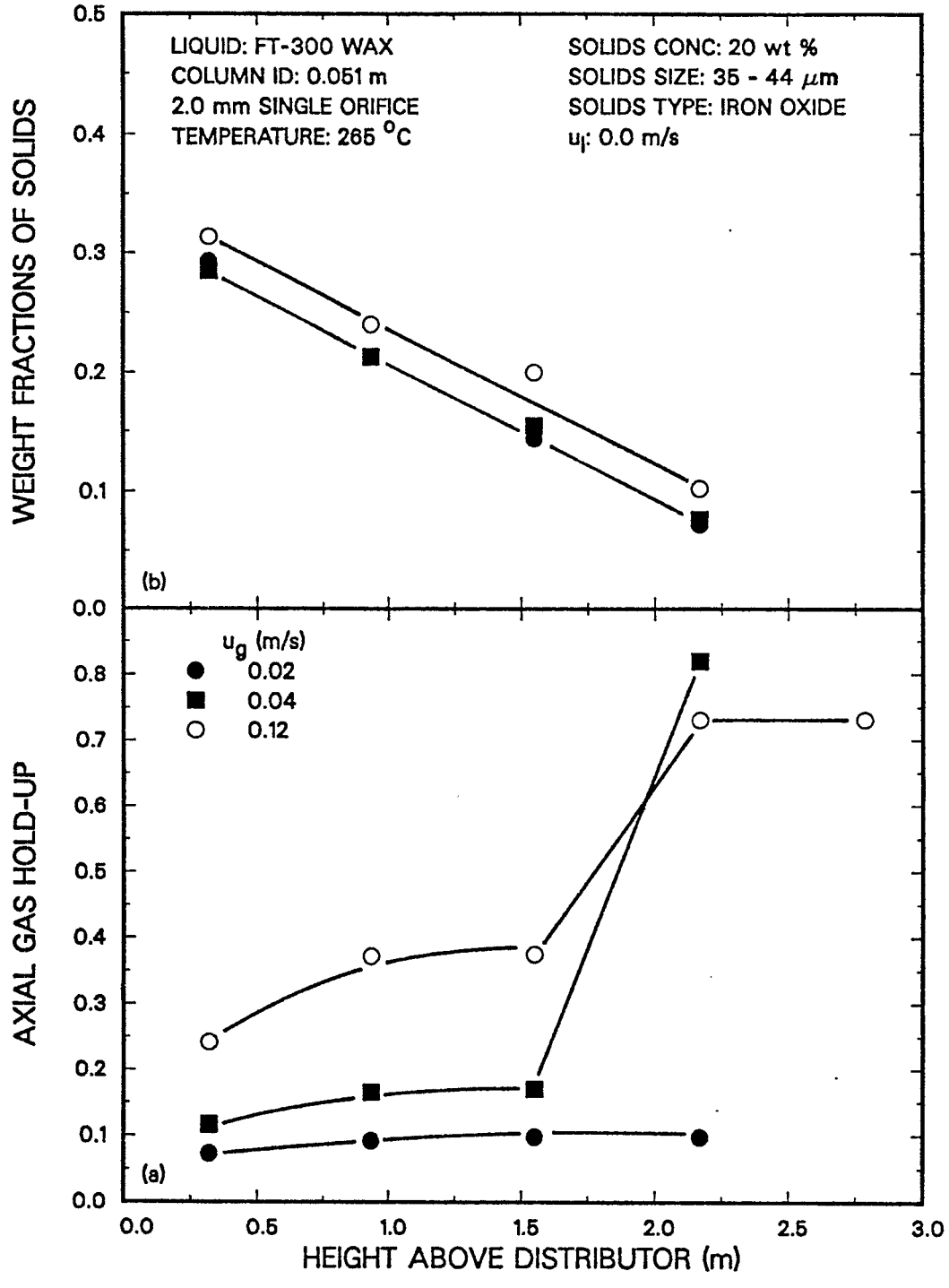


Figure 2. Effect of superficial gas velocity on axial solids distribution (top) and on axial gas hold-up (bottom).

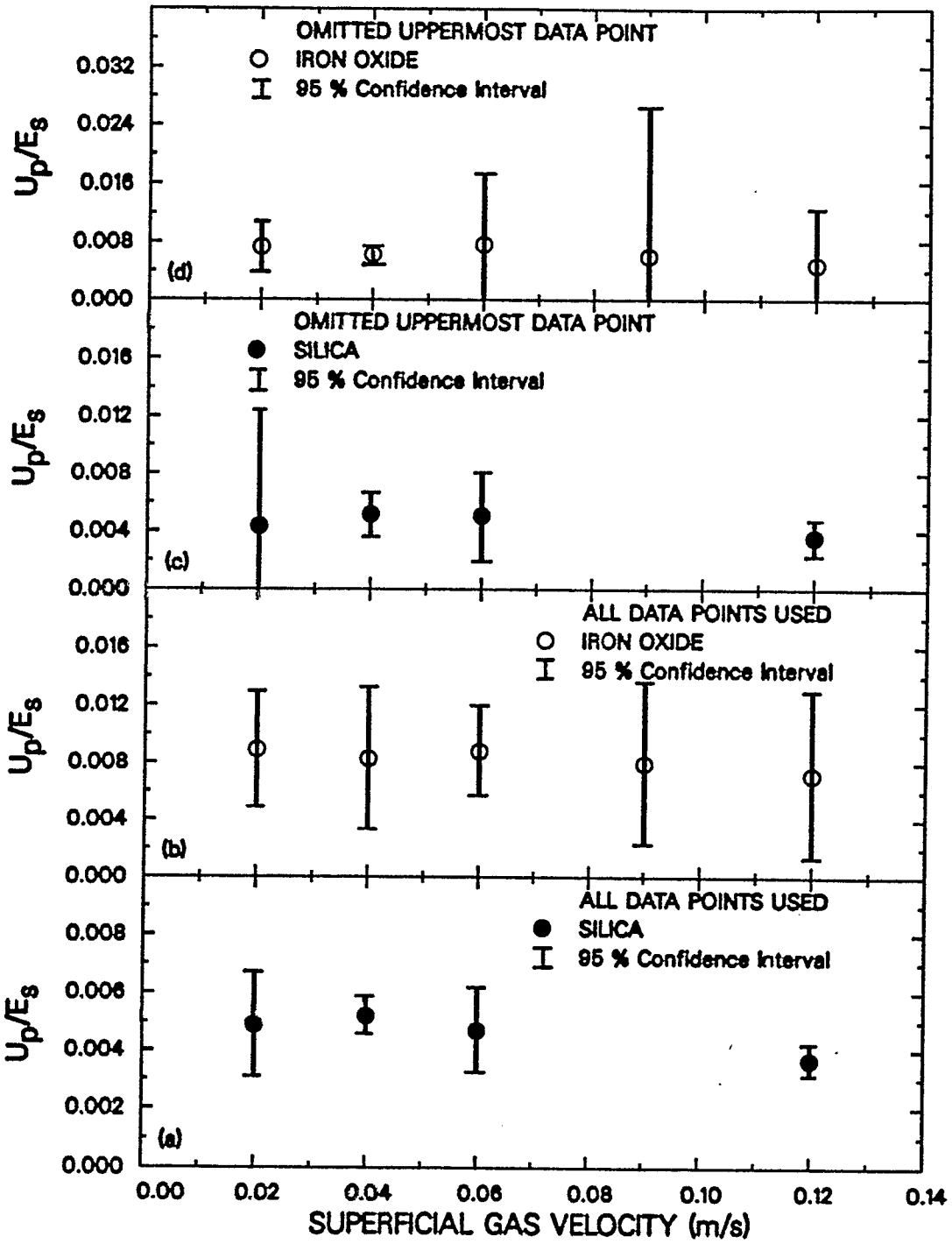


Figure 3. Effect of superficial gas velocity on $U_p/E_s$ for iron oxide (○) and silica (●) (FT-300, 265°C, $u_l = 0$ cm/s, 10, 20 wt% 20 - 44 $\mu$m $SiO_2$, 20 wt% 35 - 44 $\mu$m $Fe_2O_3$)

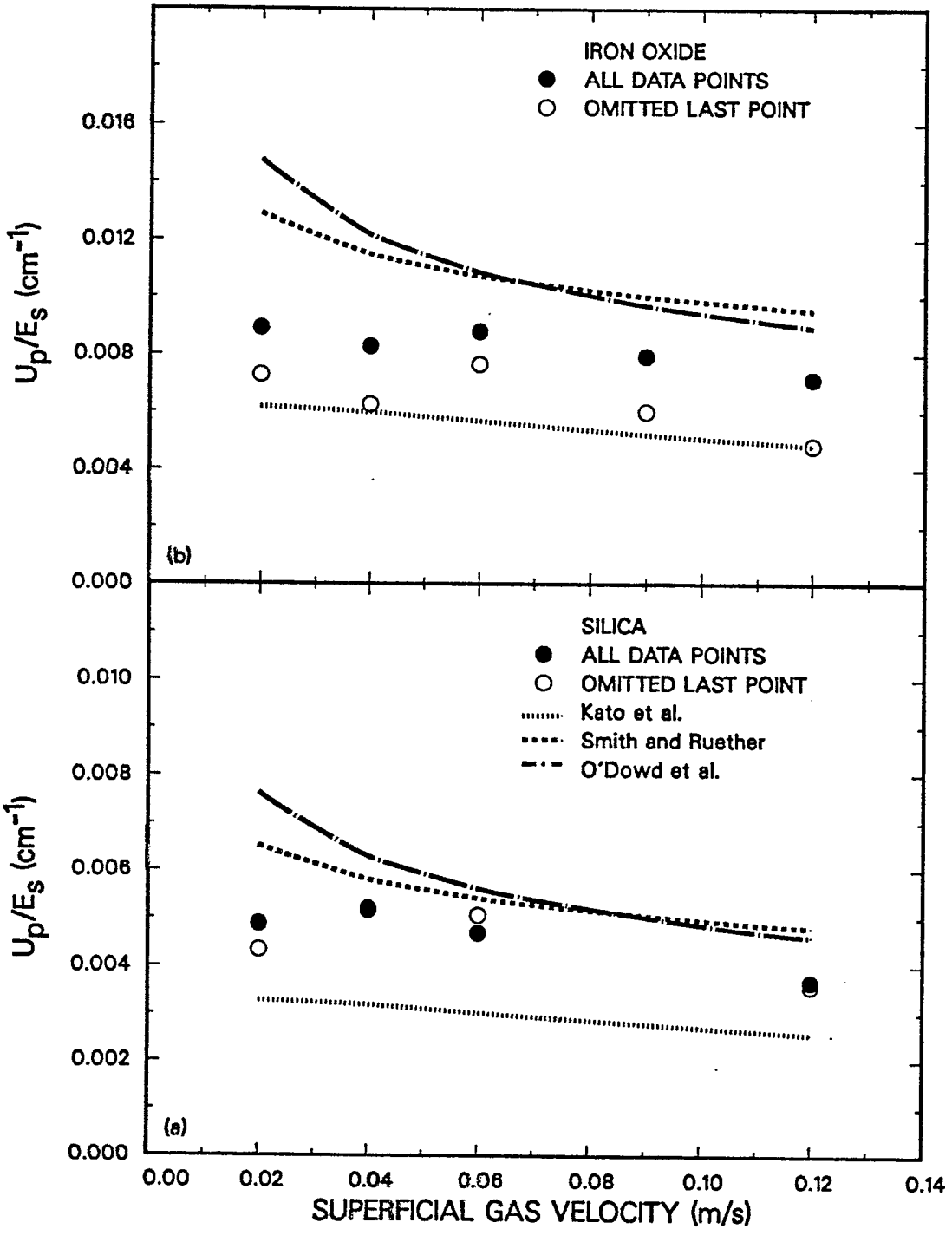


Figure 4. Comparison of $U_p/E_s$ with literature for iron oxide (top) and silica (bottom) ($T = 265^{\circ}C$, FT-300, $u_l = 0$ cm/s, 10, 20 wt% 20 – 44 $\mu$m $SiO_2$, 20 wt% 35 – 44 $\mu$m $Fe_2O_3$)

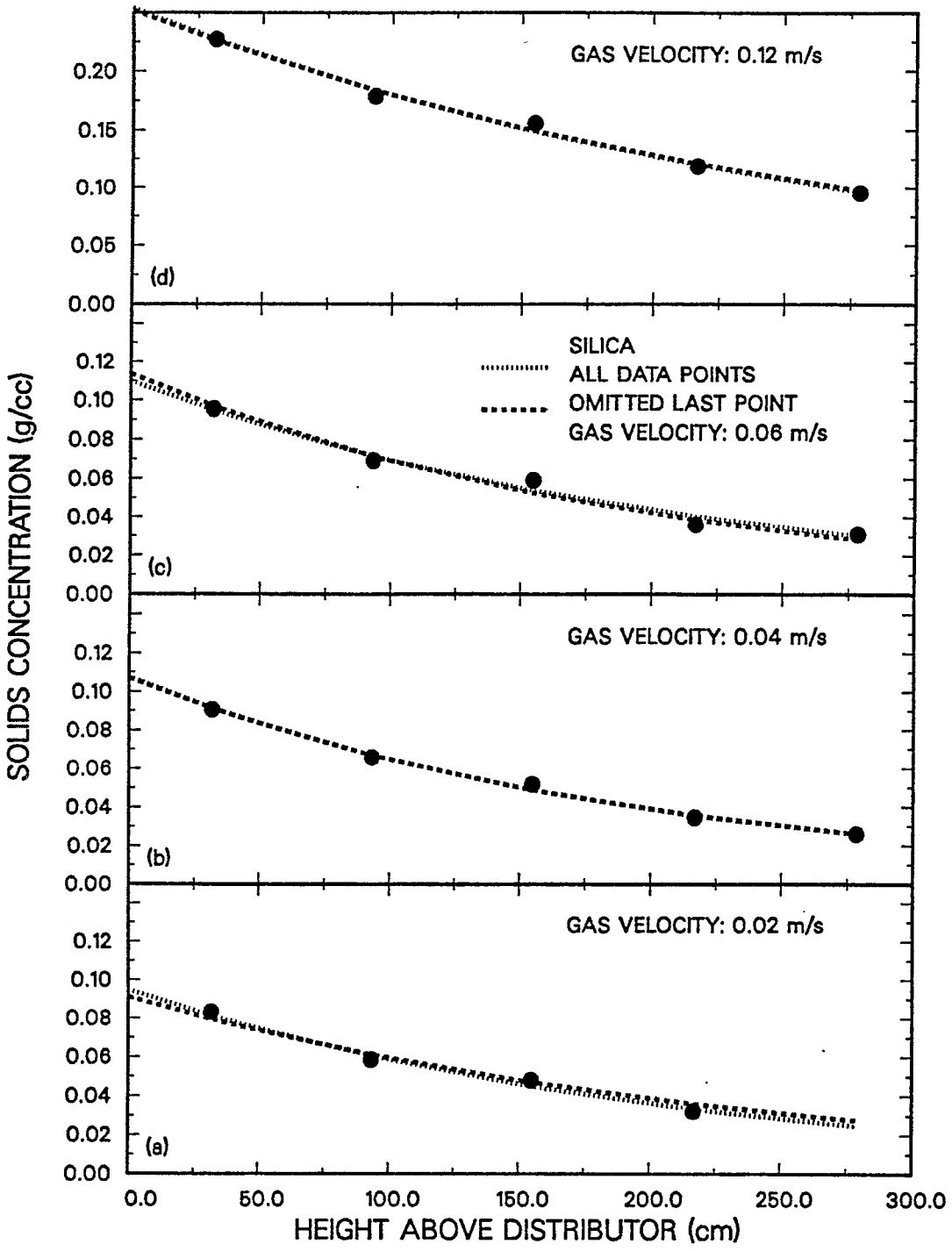


Figure 5. Axial solids concentration profiles for silica (T = 265°C, FT-300, $u_l$ = 0 cm/s, 10, 20 wt% 20 – 44 $\mu$m )

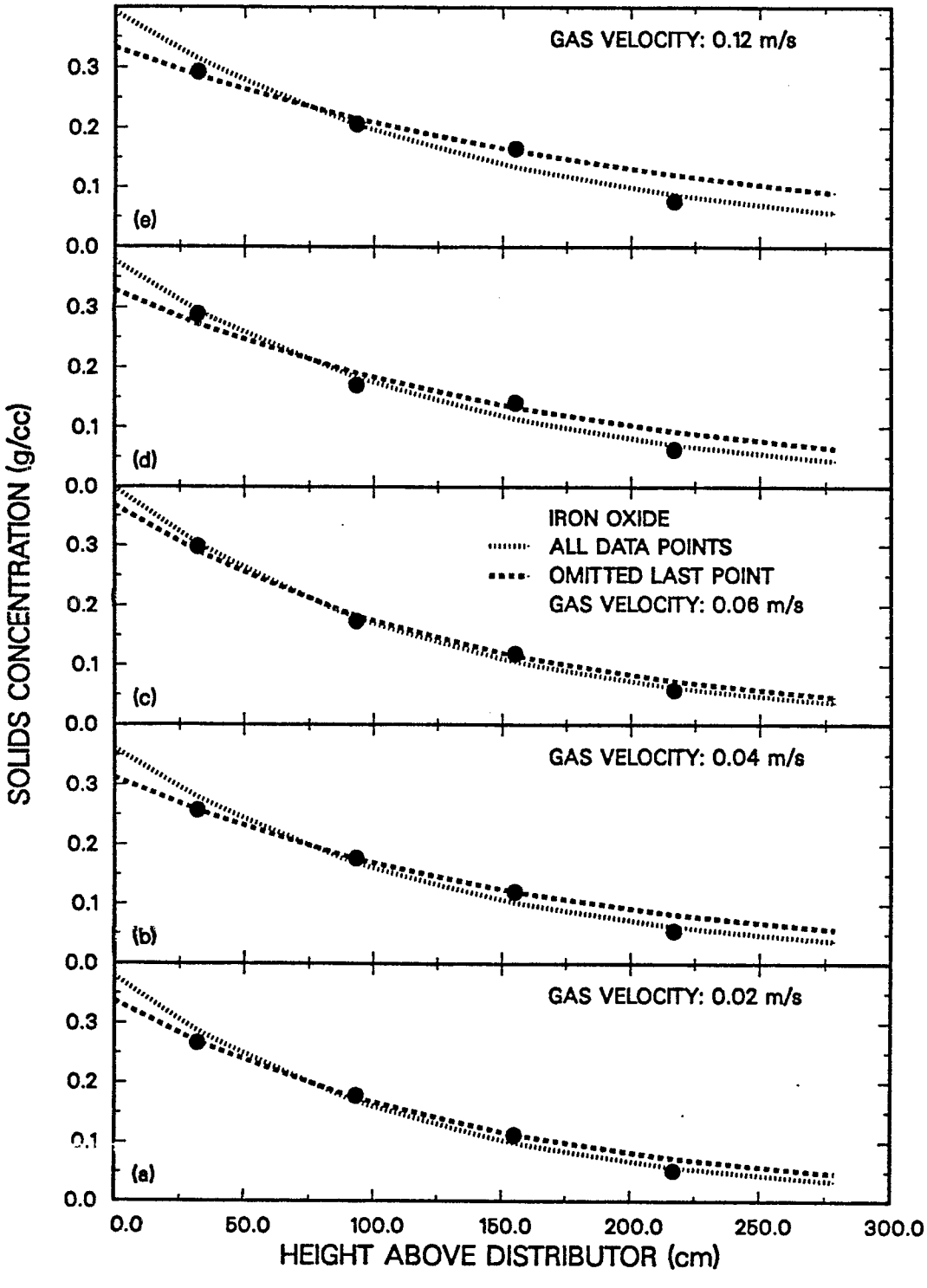


Figure 6. Axial solids concentration profiles for iron oxide (T = 265°C, FT-300, $u_l = 0$ cm/s, 20 wt% 20 - 44 $\mu$m )

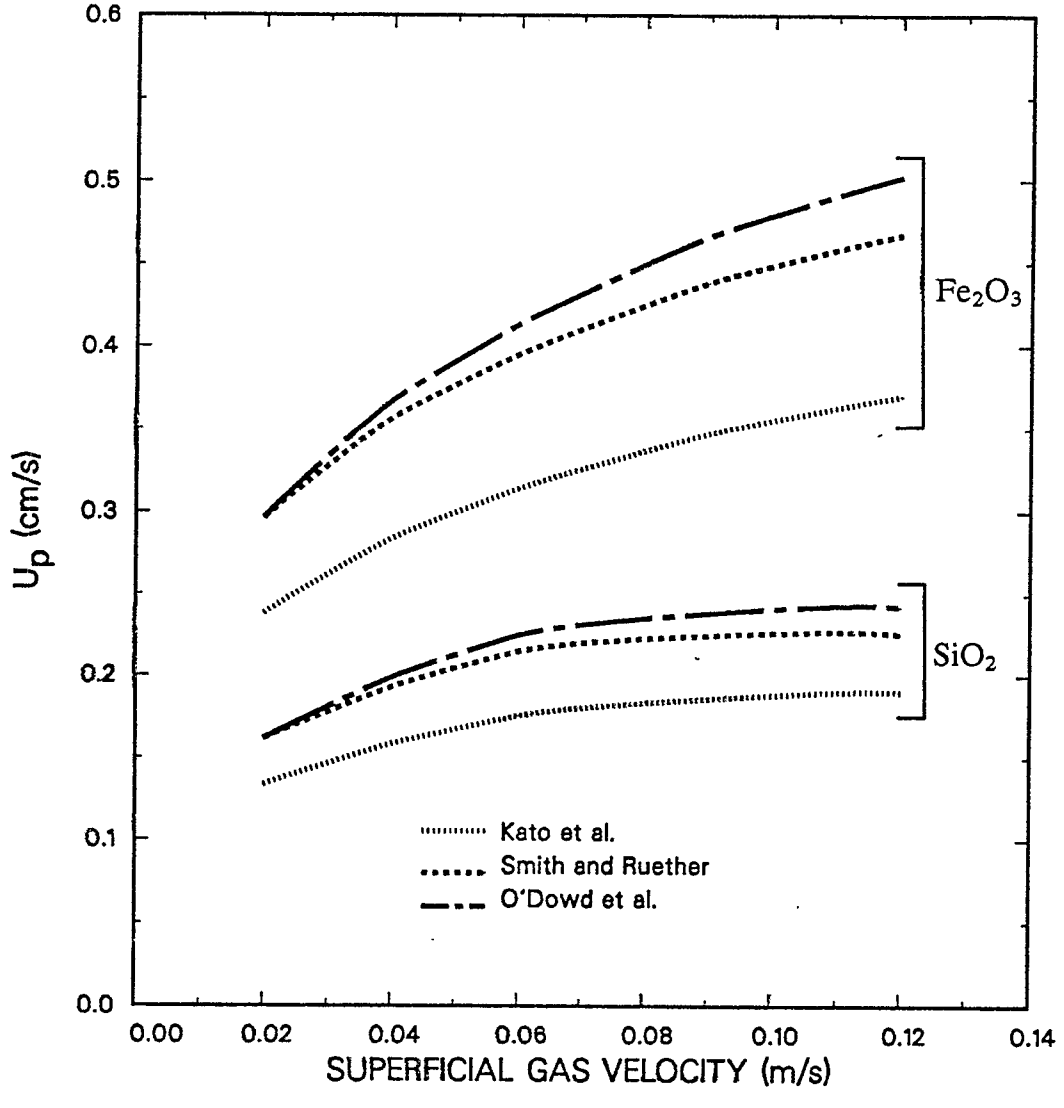


Figure 7. Effect of superficial gas velocity on hindered settling velocity for iron oxide and silica slurries based on correlations from literature

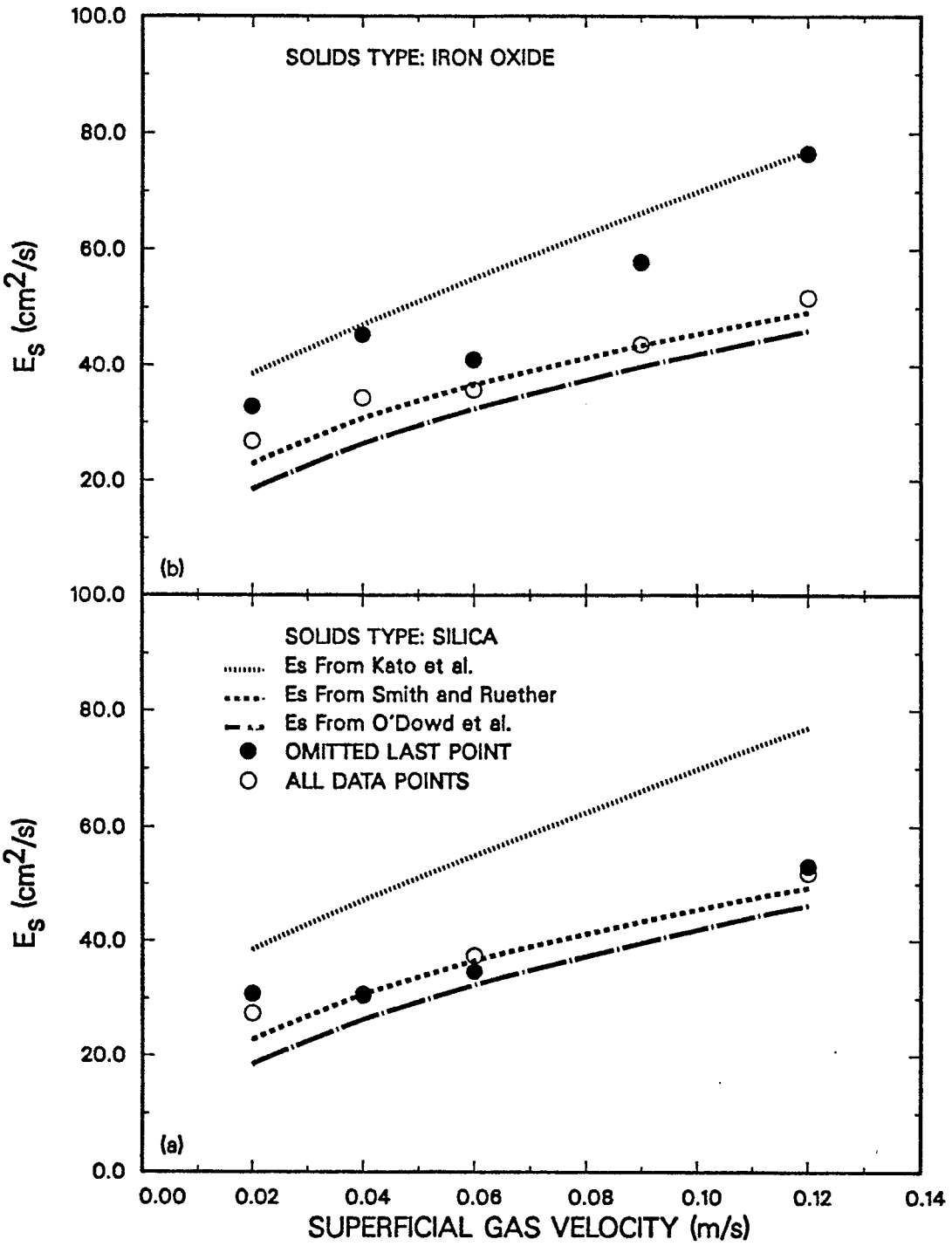


Figure 8. Effect of superficial gas velocity on axial solids dipersion coefficient for iron oxide (top) and silica (bottom) using Kato et al.'s correlation for hindered settling velocity ( T = 265°C FT-300, $u_l = 0$ cm/s, 10, 20 wt% 20 - 44 $\mu$m $SiO_2$, 20 wt% 35 - 44 $\mu$m $Fe_2O_3$)

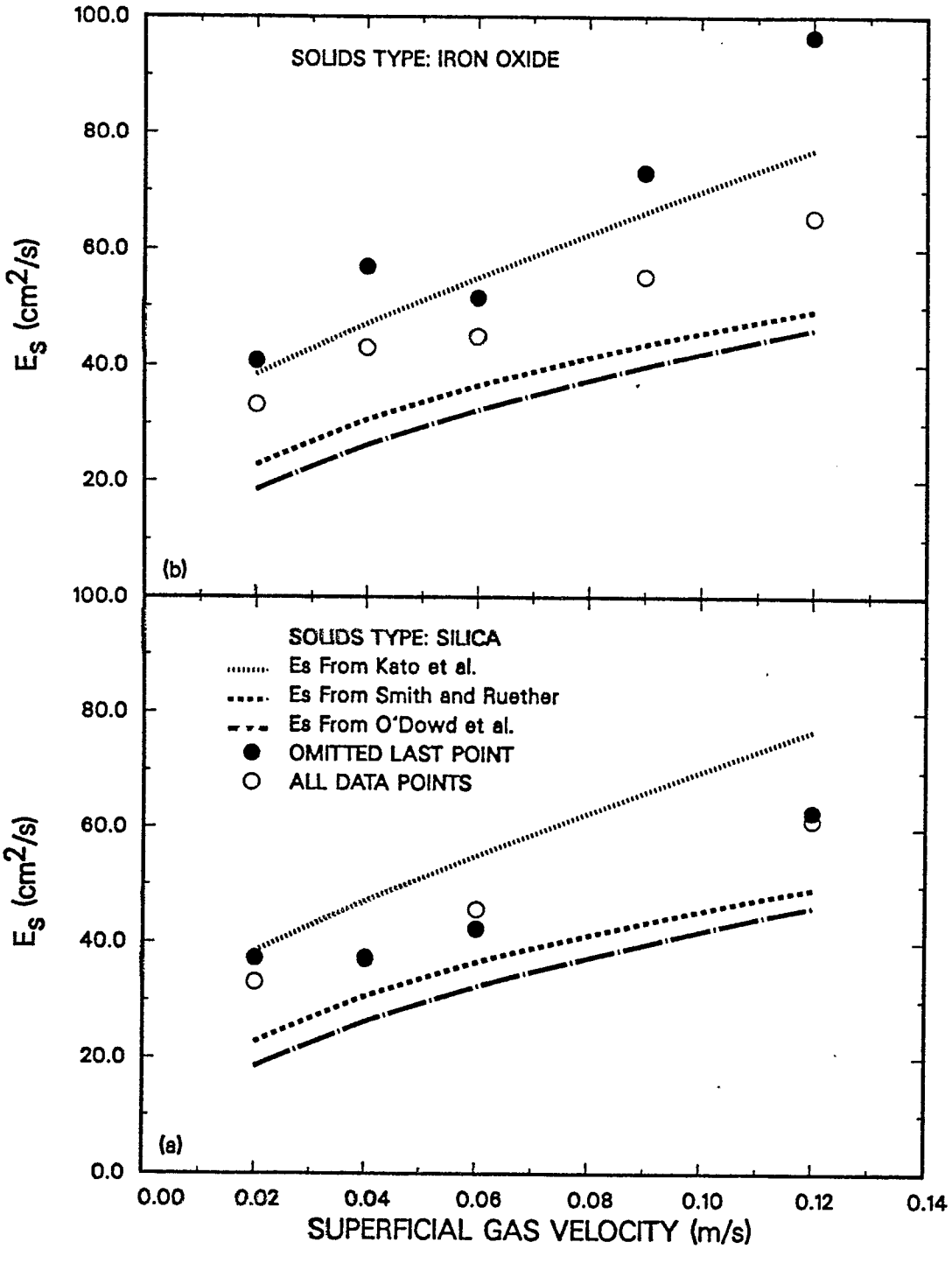


Figure 9. Effect of superficial gas velocity on axial solids dipersion coefficient for iron oxide (top) and silica (bottom) using Smith and Ruether's correlation for hindered settling velocity ( T = 265 $^{o}$C, FT-300, $u_l = 0$ cm/s, 10, 20 wt% 20 - 44 $\mu$m $SiO_2$, 20 wt% 35 - 44 $\mu$m $Fe_2O_3$)

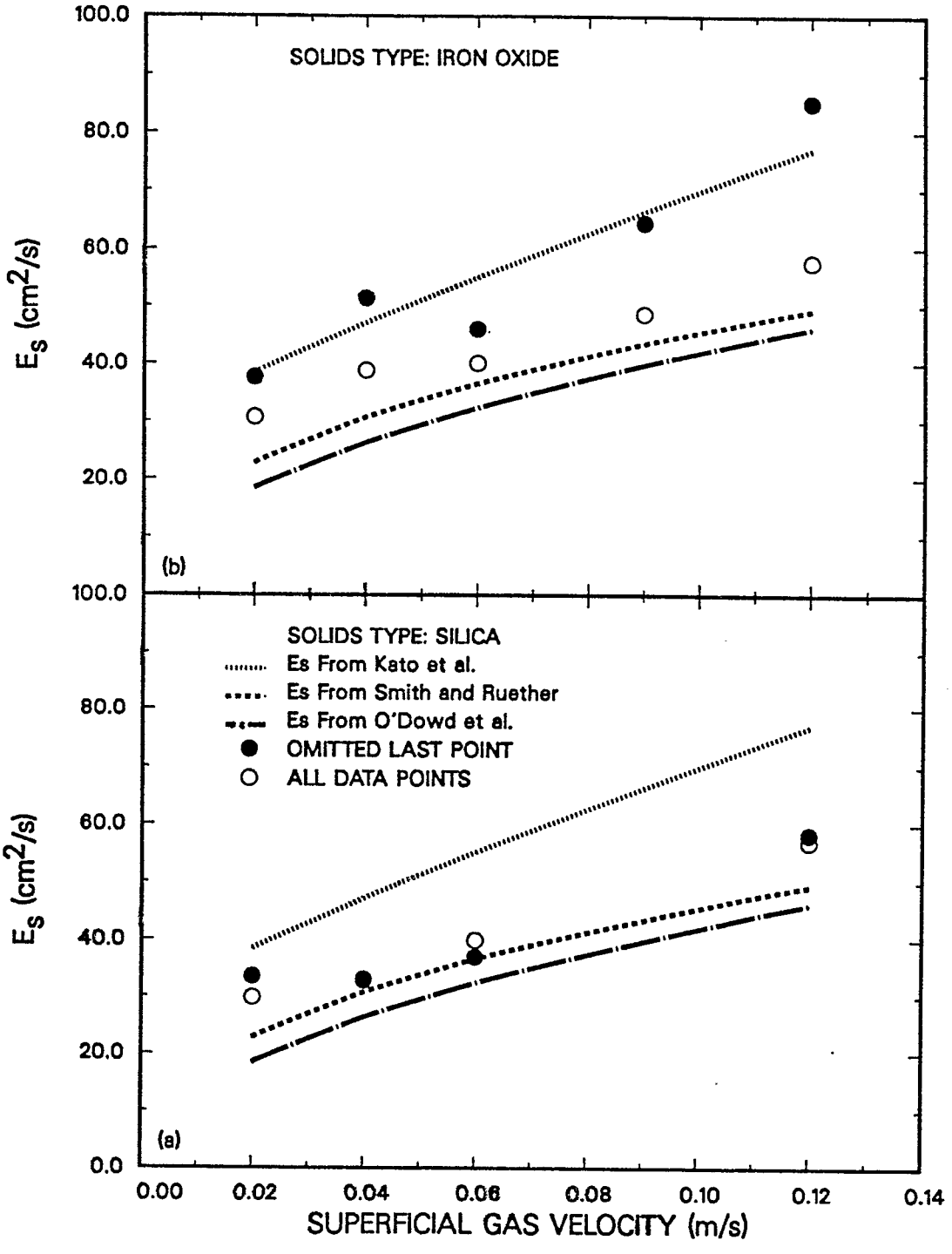


Figure 10. Effect of superficial gas velocity on axial solids dipersion coefficient for iron oxide (top) and silica (bottom) using O'Dowd et al.'s correlation for hindered settling velocity ( T = 265°C FT-300, $u_l$ = 0 cm/s, 10, 20 wt% 20 - 44 $\mu$m $SiO_2$, 20 wt% 35 - 44 $\mu$m $Fe_2O_3$)

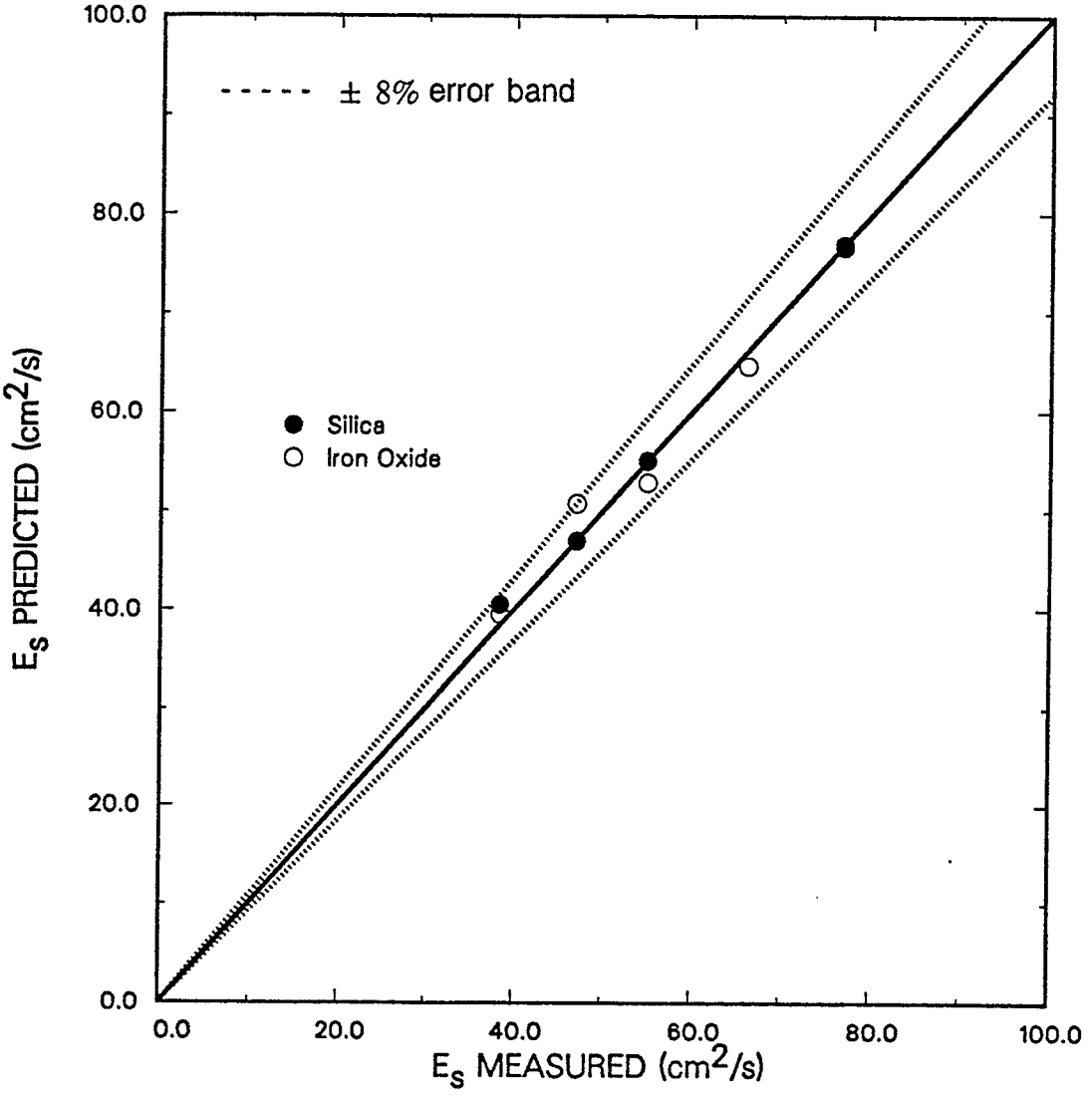


Figure 11. Parity plot comparing predicted axial solids dispersion coefficients (Eq. 7) with those obtained from the present study using a modified form of Kato et al.'s equation for hindered settling velocity ( T = 265 °C, FT-300, 10, 20 wt% 20 - 44 $\mu$m $SiO_2$, 20 wt% 35 - 44 $\mu$m $Fe_2O_3$)

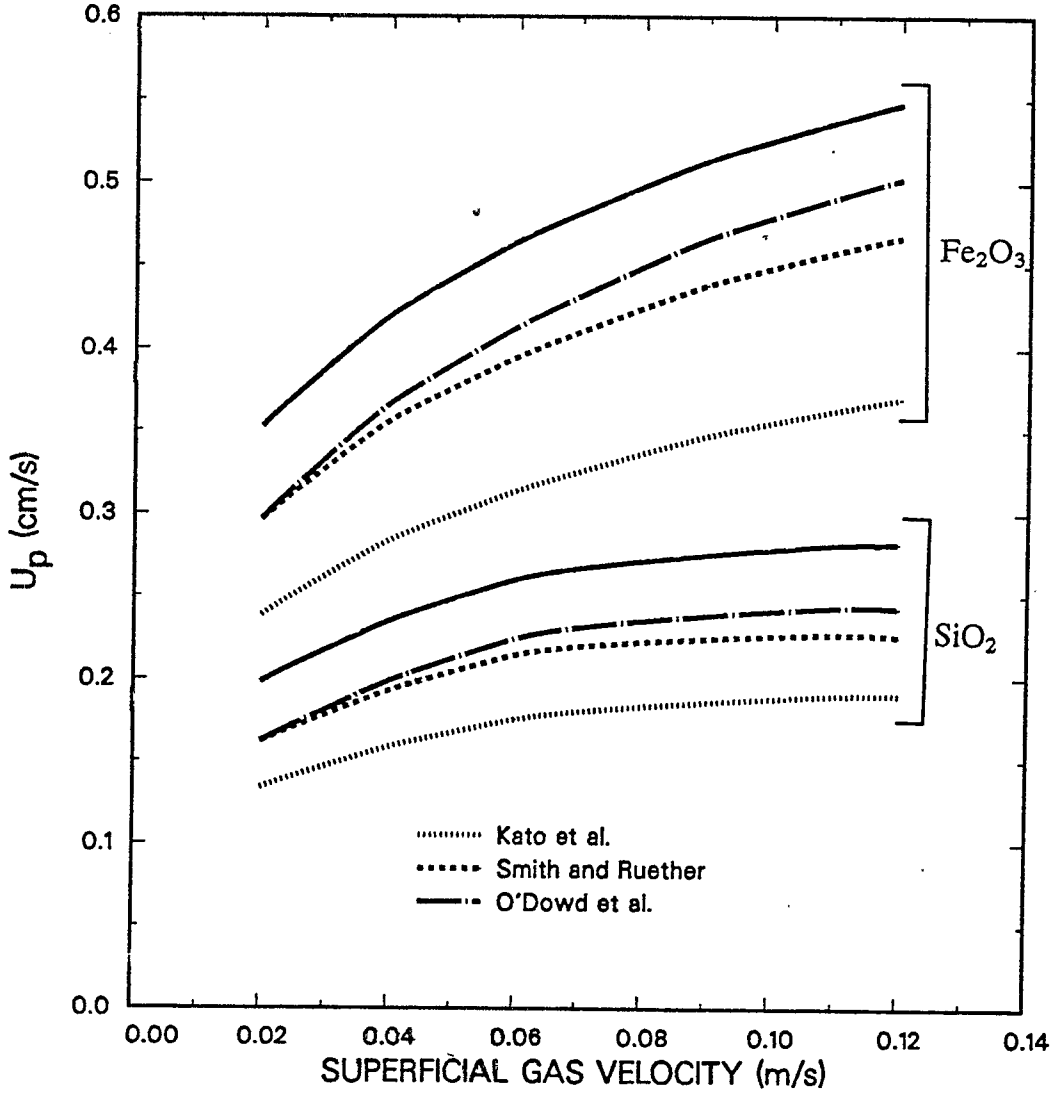


Figure 12. Effect of superficial gas velocity on hindered settling velocity for iron oxide and silica (——— settling velocities needed to satisfy Eq. 7, FT-300, T = 265 °C, $u_l$ = 0 cm/s, 10, 20 wt% 20 - 44 $\mu$m $SiO_2$, 20 wt% 35 - 44 $\mu$m $Fe_2O_3$)

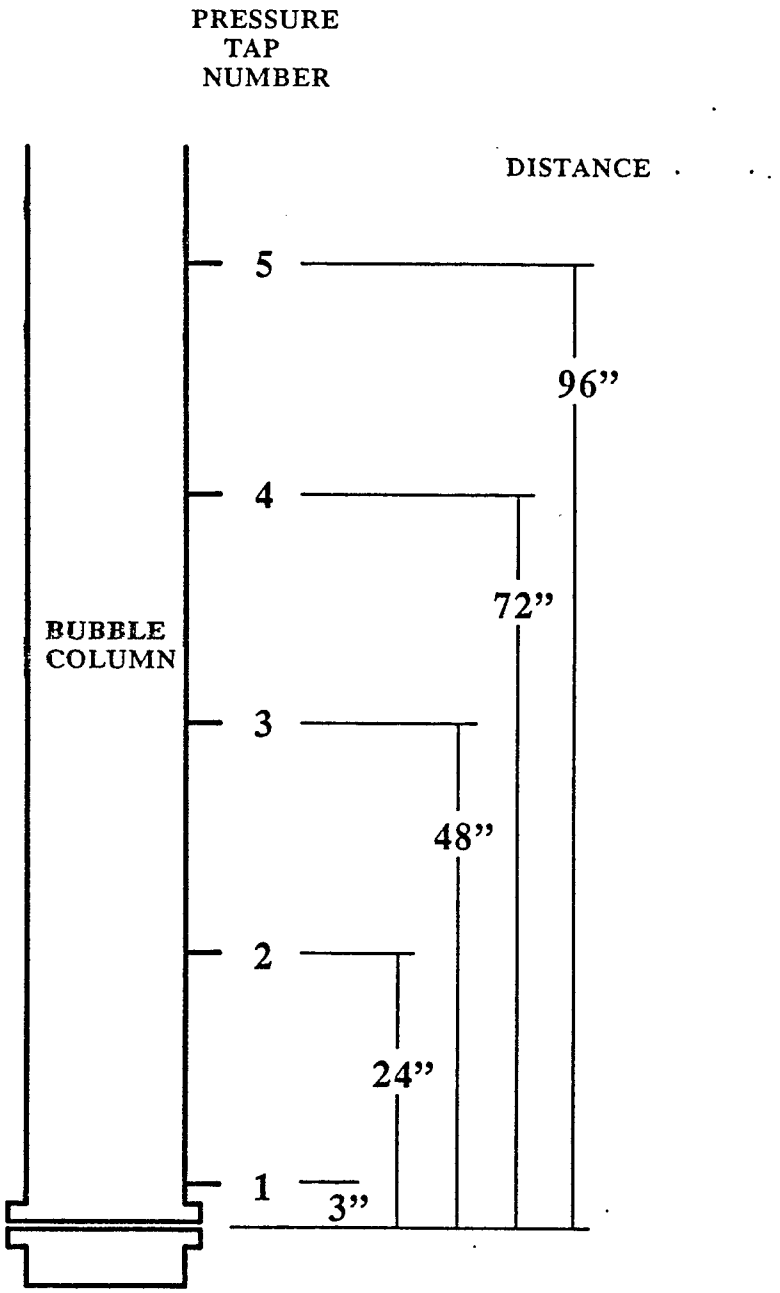


Figure 13. Schematic of pressure tap locations

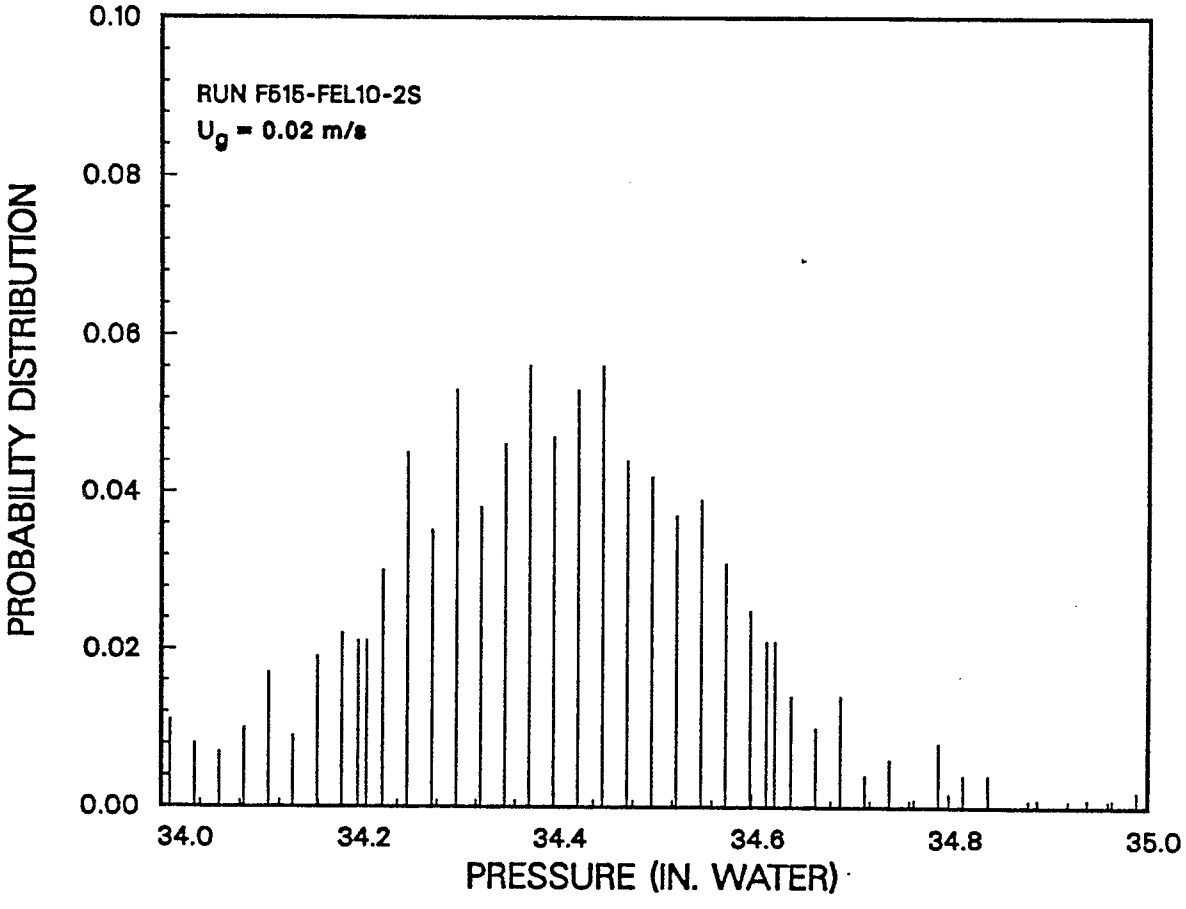


Figure 14. Probability density function for pressure fluctuations at the wall during bubbly flow (Pressure transducer #4; FT - 300, 265°C, $u_l = 0.5$ cm/s, 10 wt.% 35 - 44 $\mu$m $Fe_2O_3$, $d_c = 0.05$ m)

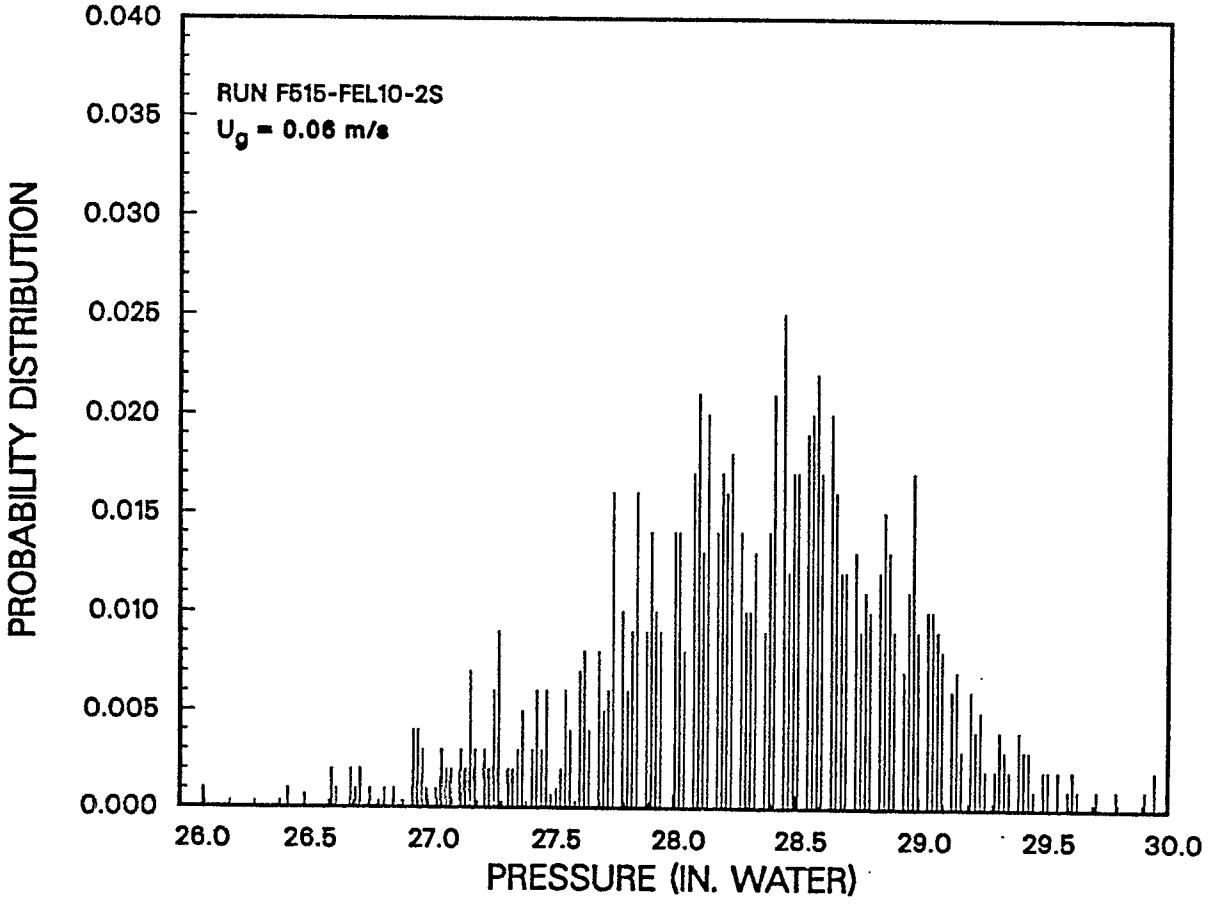


Figure 15. Probability density function for pressure fluctuations at the wall during slug flow (Pressure transducer #4; FT - 300, 265°C, $u_l = 0.5$ cm/s, 10 wt.% 35 - 44 $\mu$m $Fe_2O_3$, $d_c = 0.05$ m)

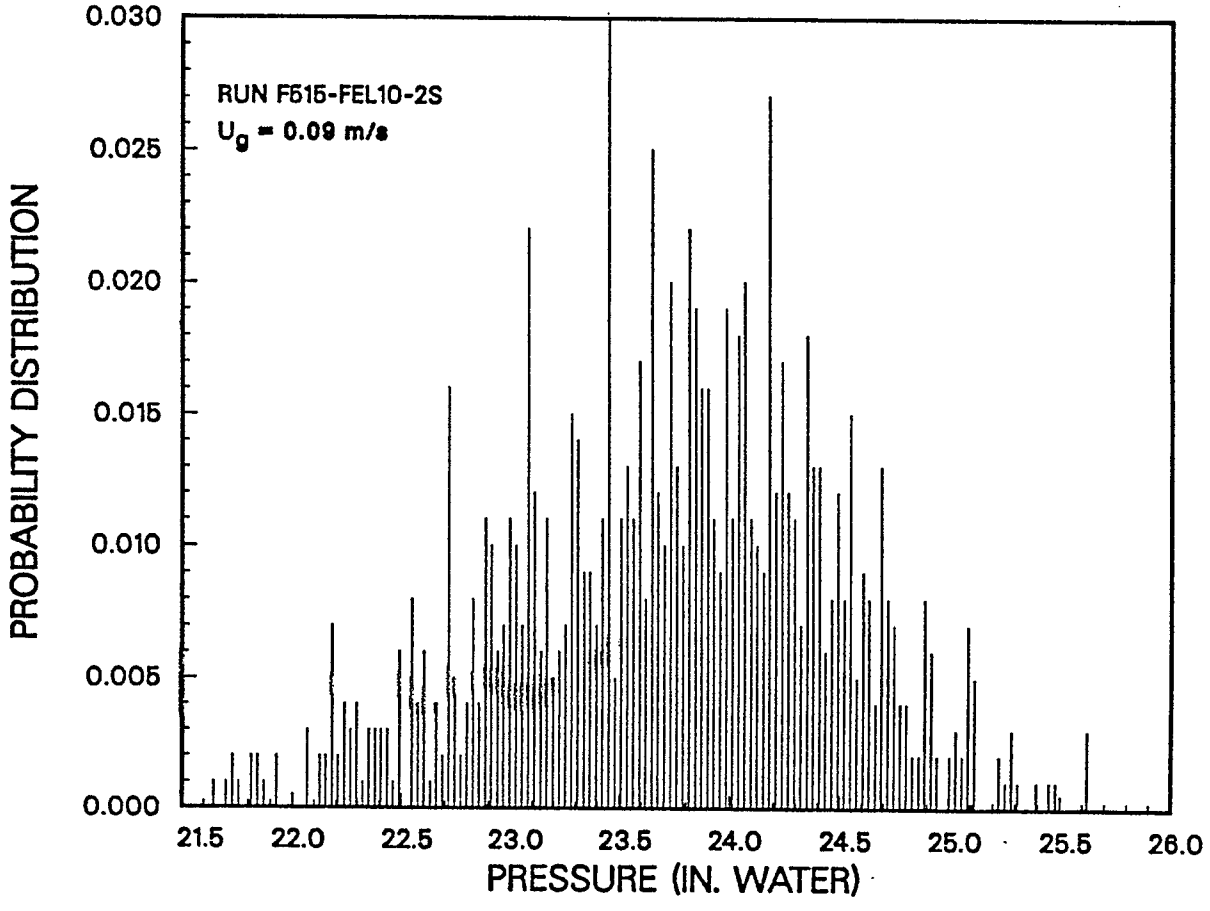


Figure 16. Probability density function for pressure fluctuations at the wall during slug flow (Pressure transducer #4; FT - 300, 265°C, $u_l = 0.5$ cm/s, 10 wt.% 35 - 44 $\mu$m $Fe_2O_3$, $d_c = 0.05$ m)

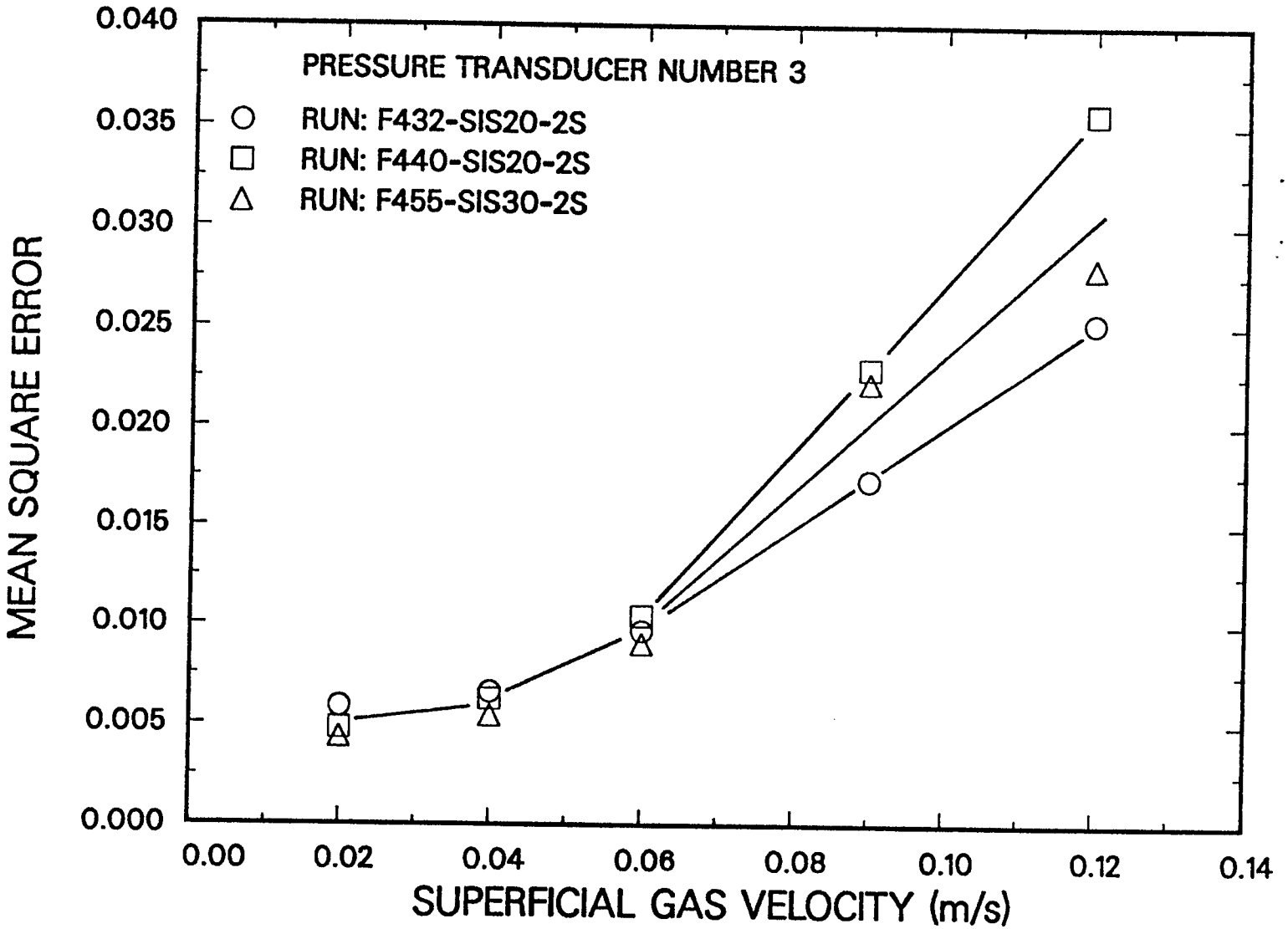


Figure 17. Effect of slurry flow rate on the mean square error of pressure fluctuations at the wall (FT–300, 265°C, 0 – 5 $\mu$m $SiO_2$, $d_c$ = 0.05 m)

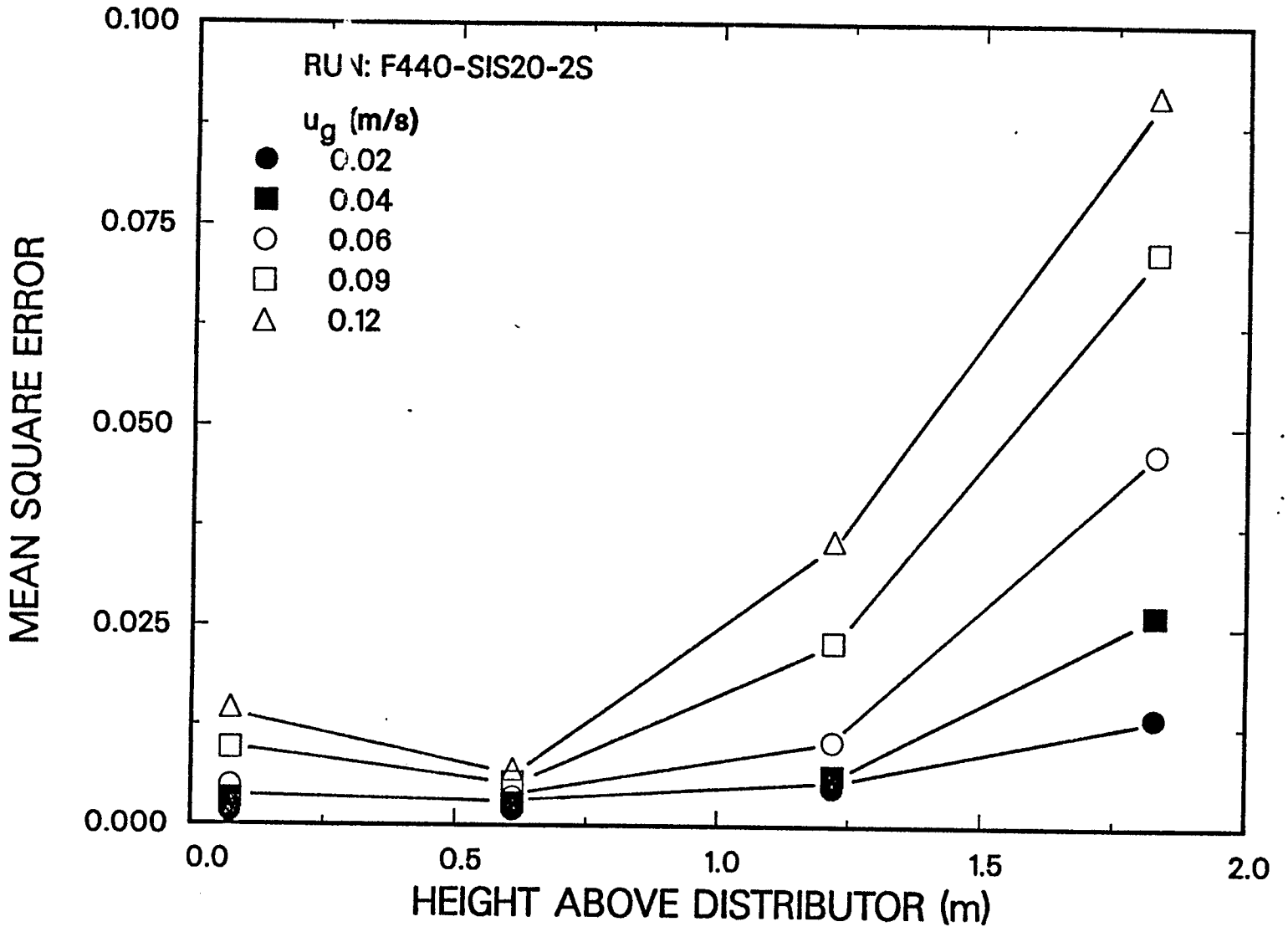


Figure 18. Effect of height above the distributor on the mean square error of pressure fluctuations at the wall (FT-300, 265°C, 20 wt.% 0 - 5 $\mu$m $SiO_2$, $d_c = 0.05$ m, $u_l = 0$ cm/s)

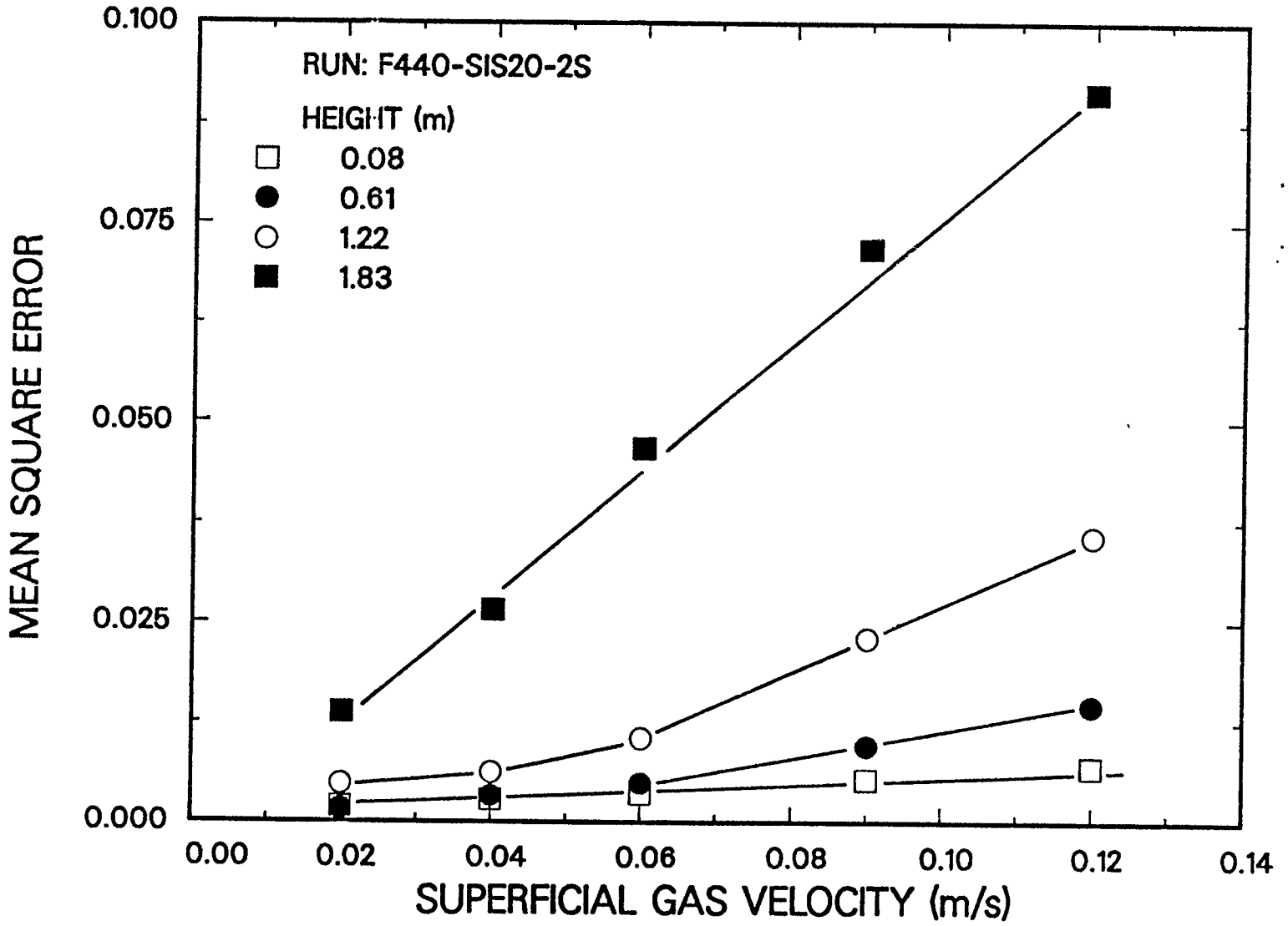


Figure 19. Effect of superficial gas velocity and height above the distributor on the mean square error of pressure fluctuations at the wall (FT-300, 265°C, 20 wt.% 0 - 5 $\mu$m $SiO_2$, $d_c = 0.05$ m, $u_l = 0$ cm/s)

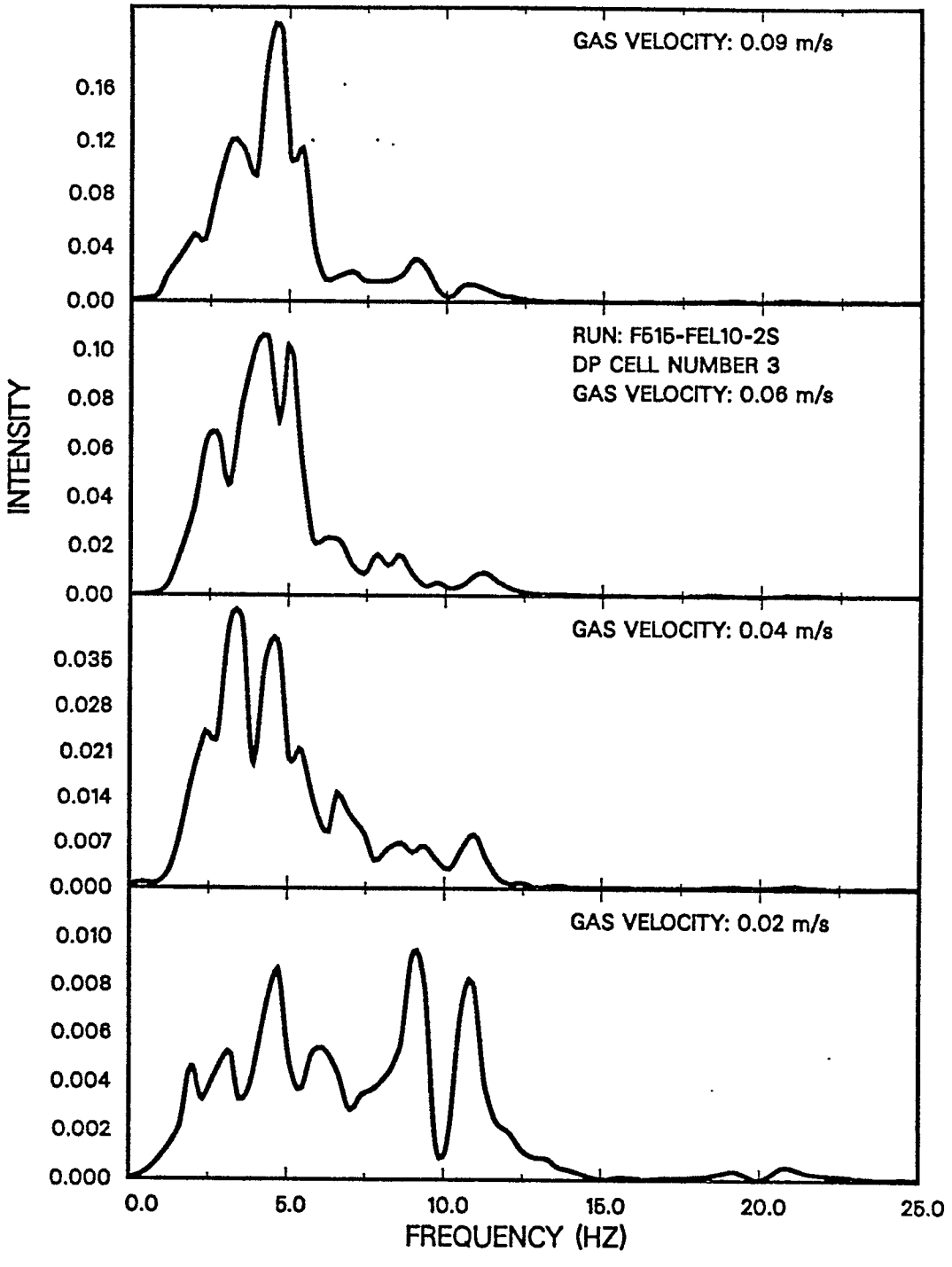


Figure 20. Effect of superficial gas velocity on the power spectral density function for pressure fluctuations at the wall (Pressure Transducer #3, FT - 300, 265°C, $u_l = 0.5$ cm/s, 10 wt.% 35 - 44 $\mu$m $Fe_2O_3$, $d_c = 0.05$ m)

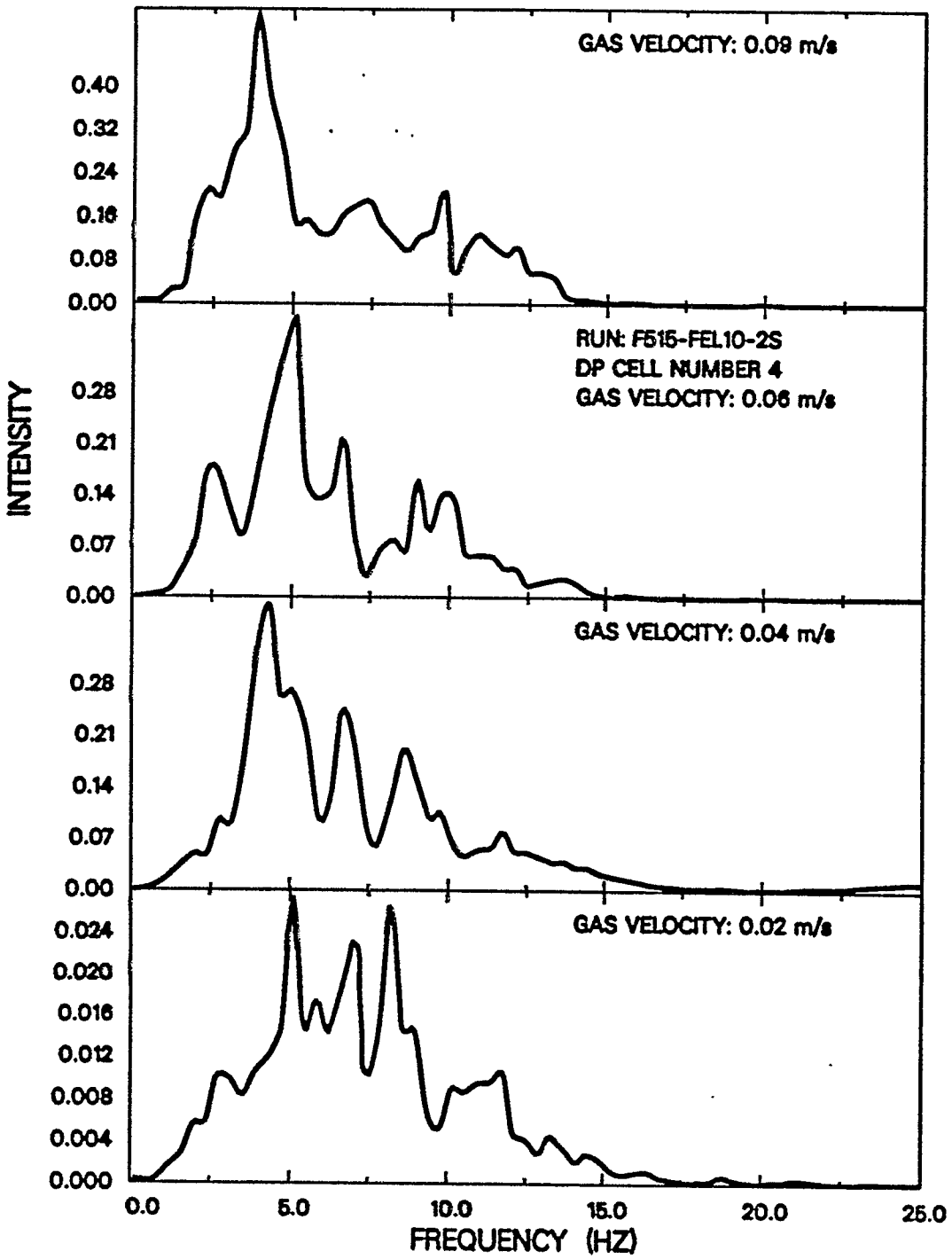


Figure 21. Effect of superficial gas velocity on the power spectral density function for pressure fluctuations at the wall (Pressure Transducer #4, FT - 300, 265°C, $u_l = 0.5$ cm/s, 10 wt.% 35 - 44 $\mu$m $Fe_2O_3$, $d_c = 0.05$ m)

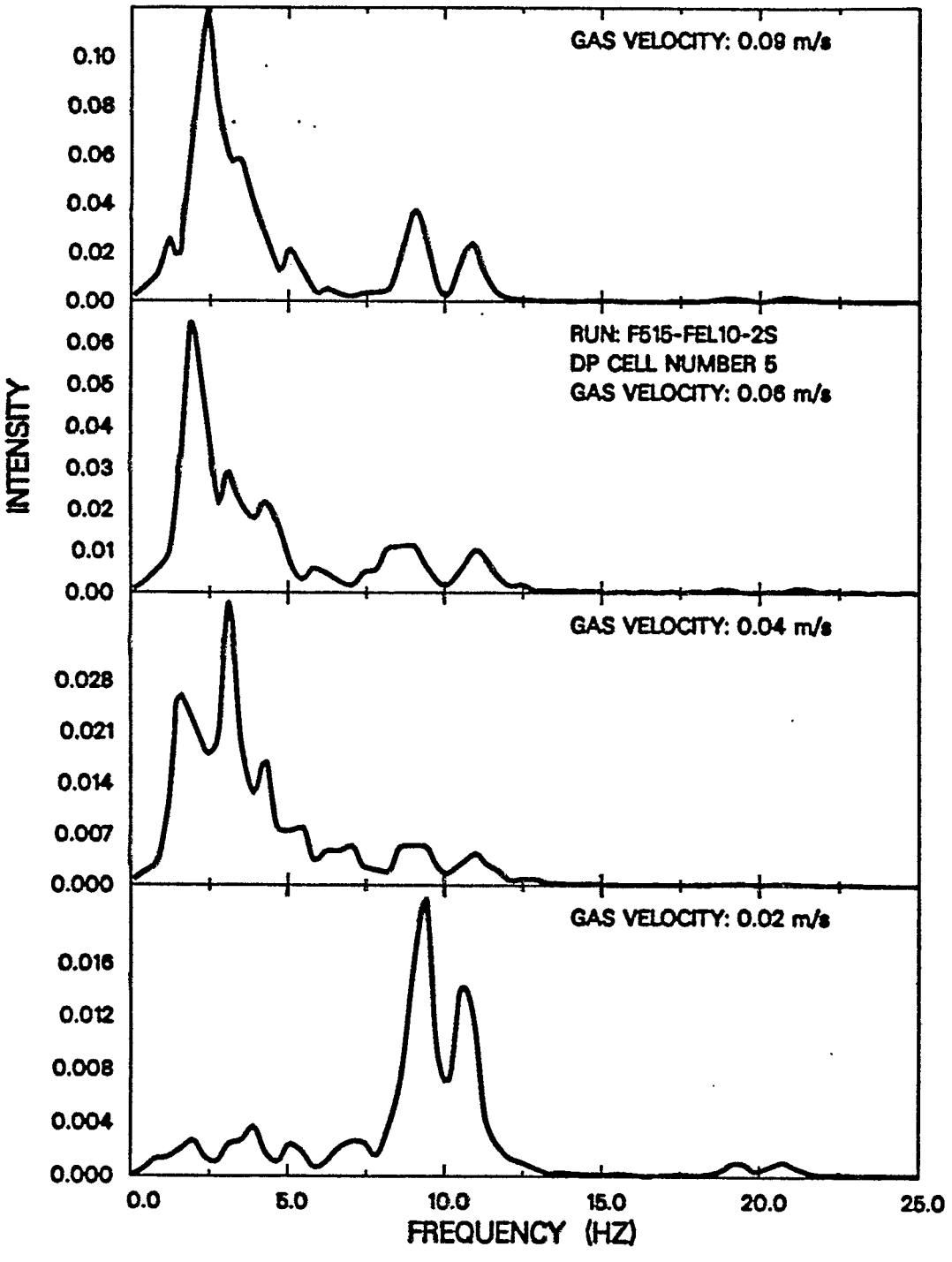


Figure 22. Effect of superficial gas velocity on the power spectral density function for pressure fluctuations at the wall (Pressure Transducer #5, FT - 300, 265°C, $u_l = 0.5$ cm/s, 10 wt.% 35 - 44 $\mu$m $Fe_2O_3$, $d_c = 0.05$ m)

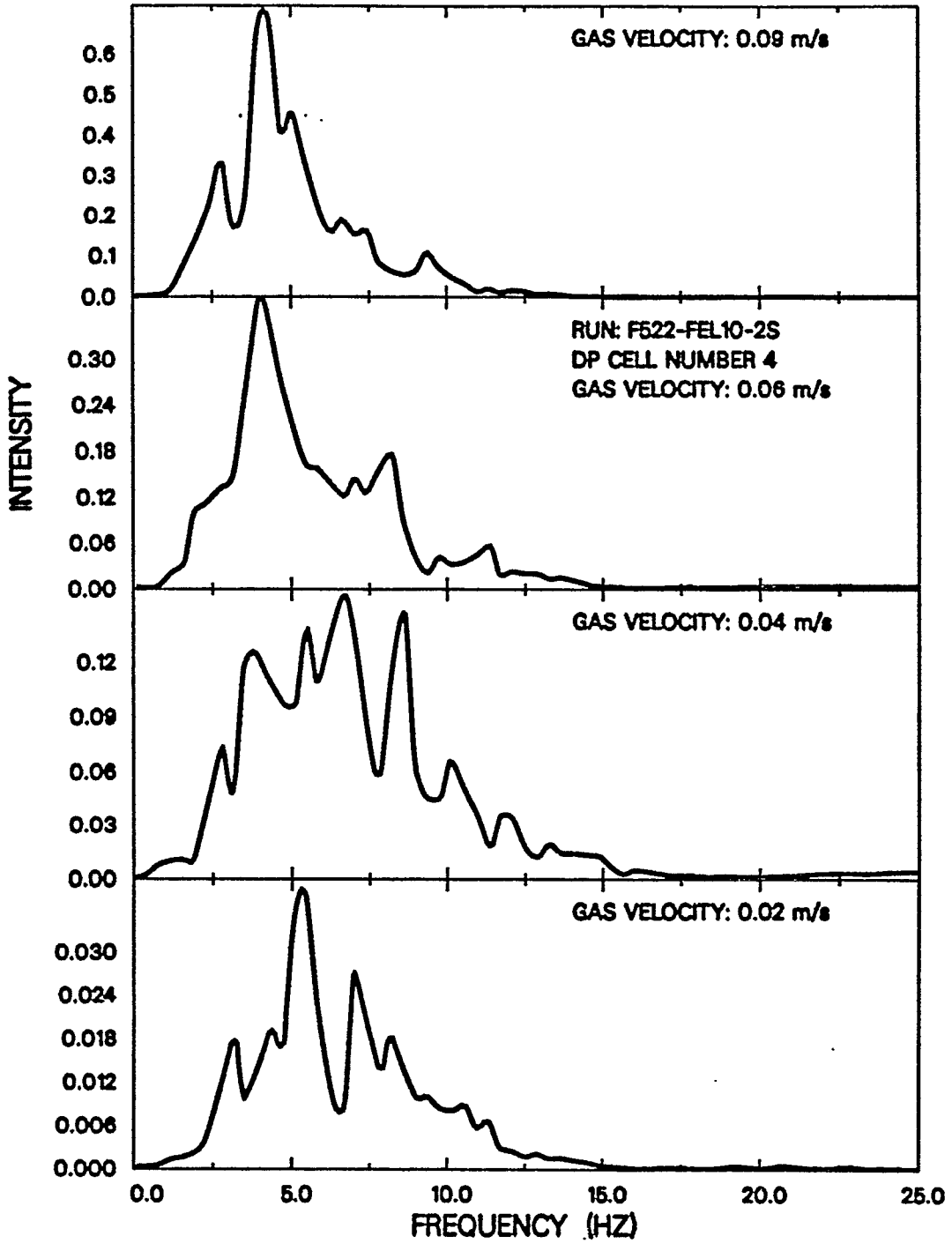


Figure 23. Effect of superficial gas velocity on the power spectral density function for pressure fluctuations at the wall (Pressure Transducer #4, FT – 300, 265°C, $u_l = 2$ cm/s, 10 wt.% 35 – 44 $\mu$m $Fe_2O_3$, $d_c = 0.05$ m)

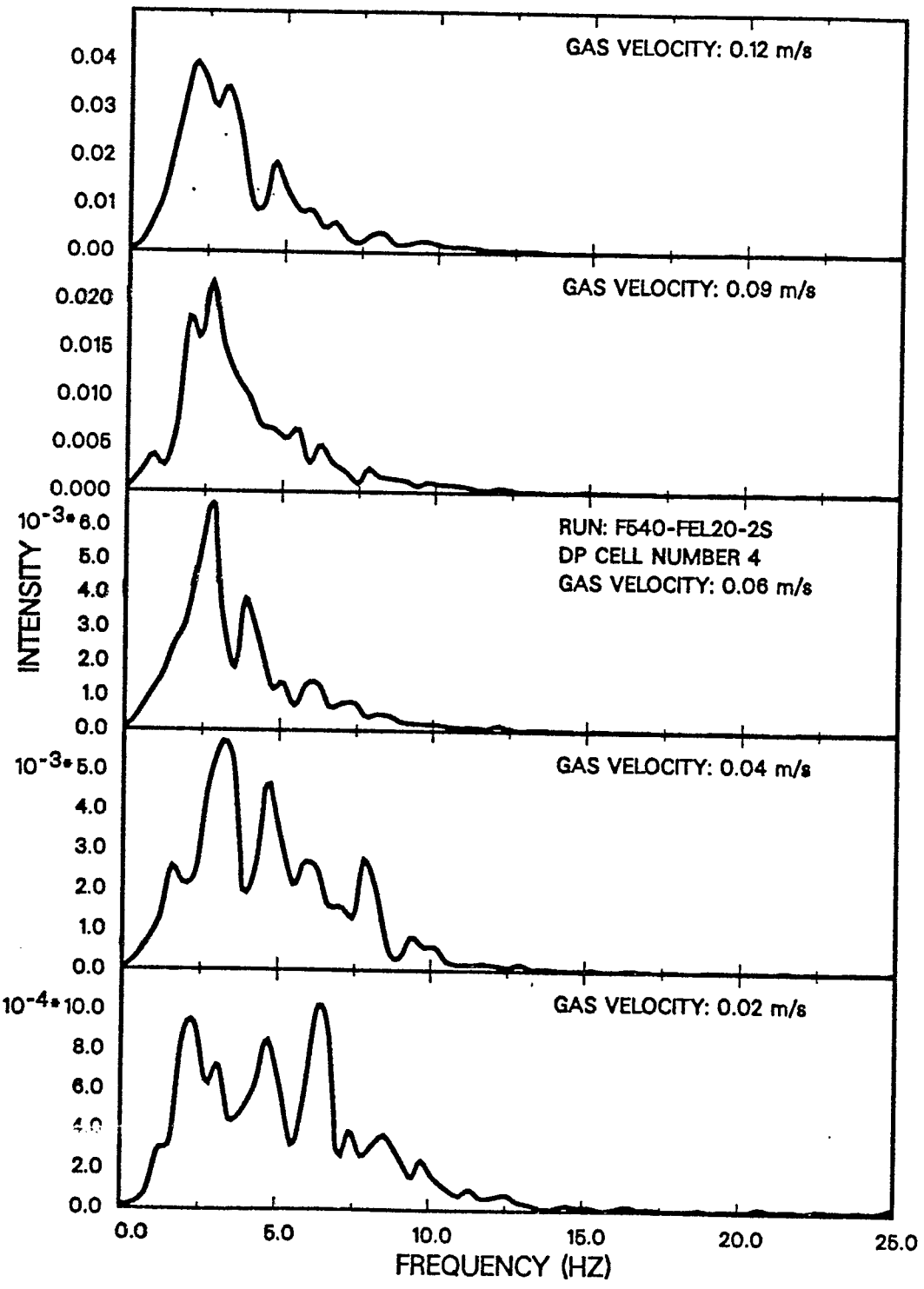


Figure 24: Effect of superficial gas velocity on the power spectral density function for pressure fluctuations at the wall (Pressure Transducer #4, FT - 300, 265°C, $u_l = 0$ cm/s, 20 wt.% 35 - 44 $\mu$m $Fe_2O_3$, $d_c = 0.05$ m)

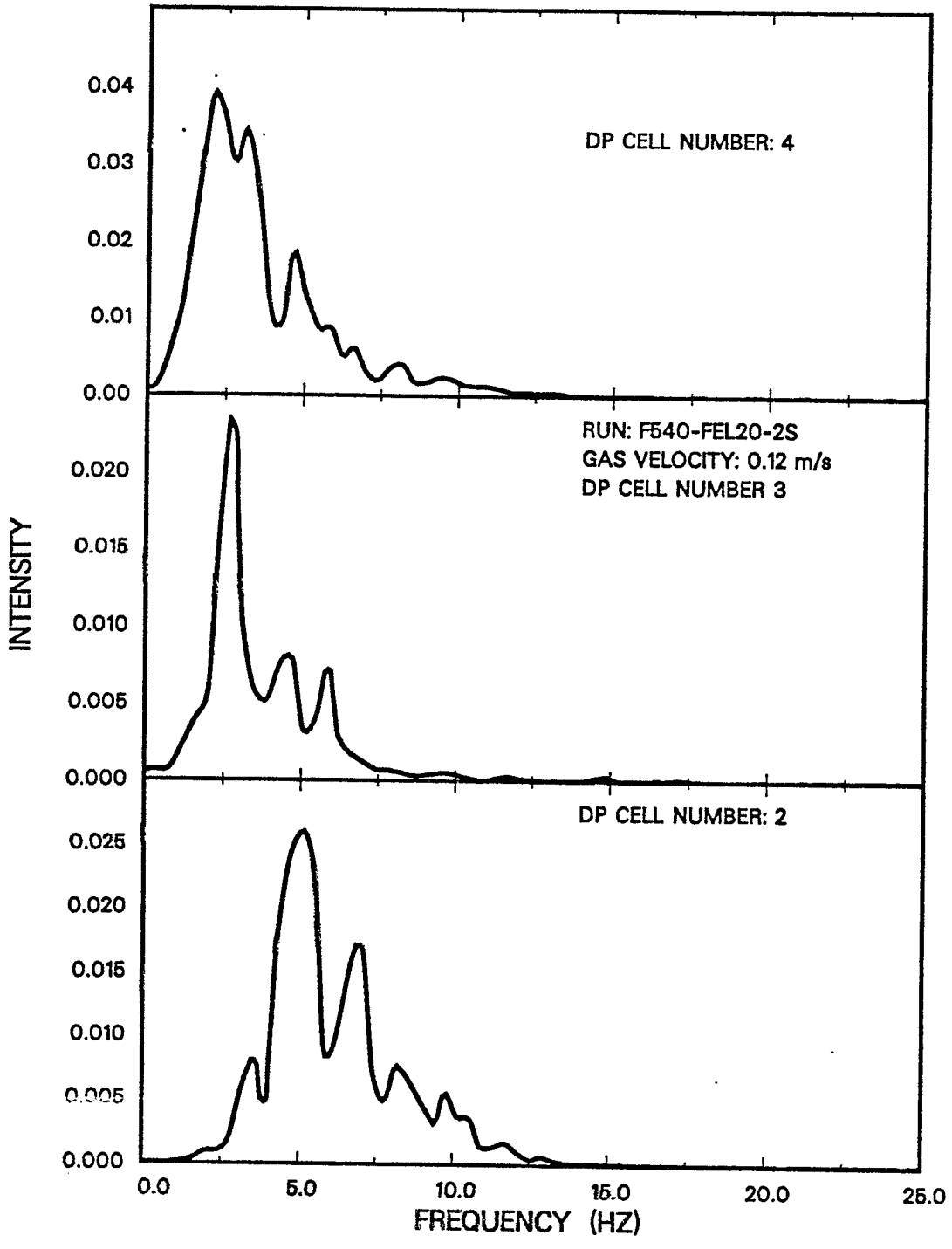


Figure 25. Effect of height above the distributor on the power spectral density function for pressure fluctuations at the wall (FT – 300, 265°C, $u_l = 0$ cm/s, 20 wt.% 35 – 44 $\mu$m $Fe_2O_3$, $d_c = 0.05$ m)

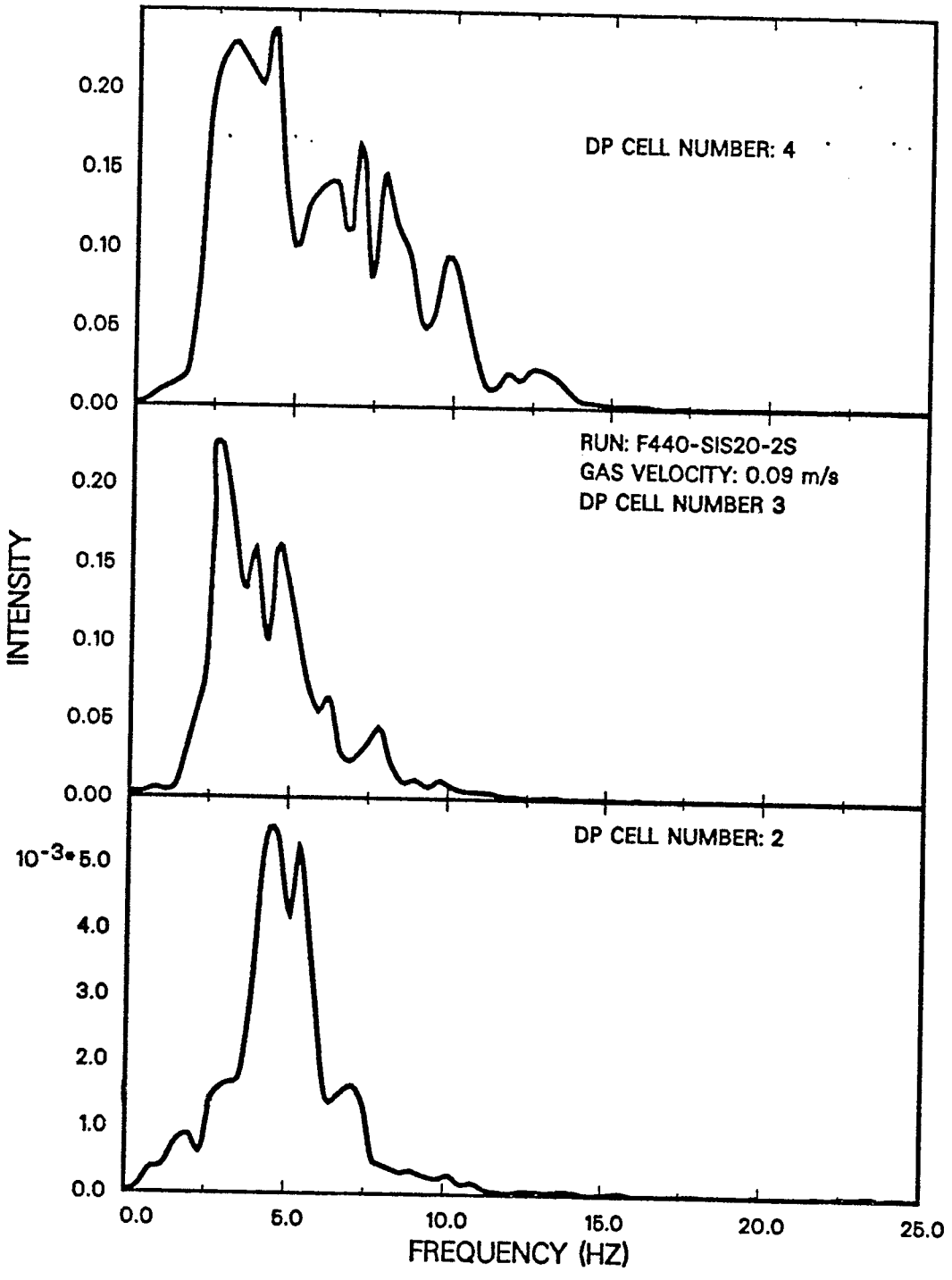


Figure 26. Effect of height above the distributor on the power spectral density function for pressure fluctuations at the wall (FT – 300, 265°C, $u_l = 0$ cm/s, 20 wt.% 0 – 5 $\mu$m $SiO_2$, $d_c = 0.05$ m)